

Simulation of potential and species distribution in a Li||Bi liquid metal battery using coupled meshes

Carolina Duczek^{a,*}, Norbert Weber^a, Omar E. Godinez-Brizuela^b, Tom Weier^a

^a*Helmholtz-Zentrum Dresden-Rossendorf, Bautzner Landstr. 400, 01328 Dresden, Germany*

^b*Norwegian University of Science and Technology (NTNU), 7030 Trondheim, Norway*

Abstract

In this work a 1D finite volume based model using coupled meshes is introduced to capture potential and species distribution throughout the discharge process in a lithium-bismuth liquid metal battery while neglecting hydrodynamic effects, focusing on the electrochemical properties of the cell and the mass transport in electrolyte and cathode. Interface reactions in the electrical double layer are considered through the introduction of a discrete jump of the potential modelled as periodic boundary condition to resolve interfacial discontinuities in the cell potential. A balanced-force like approach is implemented to ensure consistent calculation at the interface level. It is found that mass transport and concentration gradients have a significant effect on the cell overpotentials and thus on cell performance and cell voltage. By quantifying overvoltages in the Li||Bi cell with a mixed cation electrolyte, it is possible to show that diffusion and migration current density could have counteractive effects on the cell voltage. Furthermore, the simulated limiting current density is observed to be much lower than experimentally measured, which can be attributed to convective effects in the electrolyte that need to be addressed in future simulations.

The solver is based on the open source library OpenFOAM and thoroughly verified against the equivalent system COMSOL multiphysics and further validated with experimental results. It is openly available at <https://doi.org/10.14278/rodare.2313>.

Keywords: OpenFOAM, liquid metal battery, molten salt battery, species transfer

1. Introduction

1.1. Liquid metal battery and its application

Due to the transition from fossil fuel and nuclear energies to renewables, the demand for stationary grid scale energy storage is increasing. Grid fluctuations

*Corresponding author

Email address: c.duczek@hzdr.de (Carolina Duczek)

need to be balanced out and peak demands must be supplied.

The liquid metal battery (LMB) has the potential to meet the requirements of durability, high power, energy efficiency and low cost and therefore is a highly promising storage technology. Basically, LMBs consist of two liquid electrodes and a molten salt electrolyte. The positive electrode – or cathode – is a heavier metal, while the negative electrode – or anode – is a lighter one¹. The electrode materials – mainly being earth-abundant and inexpensive – are selected in a manner such that they are liquid at the operating temperature while having a sufficiently large density difference. When the system is heated, the components self segregate into three immiscible horizontal layers. Moreover, the liquid state and the high temperatures enable superior kinetics and transport properties. At the same time, dendrite growth and electrolyte fracture – which are challenging in solid-state batteries – are avoided. On the other hand, the high operating temperatures are disadvantageous and increase risk and speed of corrosion. Sensitivity against motion, which can result in short circuits, makes the technology unsuitable for portable applications and restricts LMBs to stationary storage [1, 2].

There are many possible material pairings available, of which the lithium-bismuth cell has been investigated most intensively and therefore, most material properties are readily available [3]. The basic working principle at discharge of a Li||Bi LMB is shown in Fig. 1. First, the anode metal lithium is oxidised at

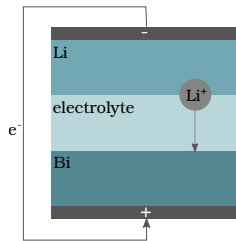


Figure 1: Schematic of a Li||Bi LMB upon discharge.

the anode-electrolyte interface and then the Li^+ ion is transported through the electrolyte. Thereafter, the lithium ion is reduced at the electrolyte-cathode interface, alloys with the solvent metal bismuth and diffuses into the cathode. The process is reversed when the cell is charged.

Motivated by the imminent risk of short circuits – caused by strong fluid flow in the completely liquid cell – much theoretical and numerical work has been devoted to LMB fluid dynamics in the past. Especially, coupling the different regions with the fundamental equations of electrochemistry, fluid dynamics, electromagnetics and heat transport is a challenging task. In LMBs, different phenomena resulting from mass transport, heat transfer and (magnetohydro-

¹In the present paper, “cathode” will always be used for the positive electrode and “anode” for the negative one since the discharge behaviour is investigated only.

dynamically) induced flow are occurring simultaneously and heavily influence each other as well as the battery performance [4]. As described in the review by Kelley and Weier [5], the investigated fluid flow phenomena include thermal convection [6–12], Marangoni convection [9], interfacial instabilities [13–19], the Taylor instability [20–24] and electro-vortex flow [8, 12, 19, 25, 26].

Cell efficiency is, in addition to short-circuits, the second most important research topic. Generally, the cell voltage of LMBs is determined by the open-circuit potential and various overpotentials, which are typically divided into three groups: (i) ohmic losses, (ii) mass transfer overpotentials caused by concentration gradients and (iii) charge transfer losses. Already 60 years ago, it was predicted that the latter will be negligible at liquid-liquid interfaces [27] – a fact, which is still valid today [28]. While during the first years of LMB research it was thought that ohmic losses in the electrolyte represent the only [27, 29], or at least major overpotential [30, 31], it was found soon that concentration polarisation can as well be important [32–34] – especially when applying high current densities [27, 35]. The maximum cell current is known to be limited by mass transfer [36, 37]. While these experimentally observed polarisation effects were attributed to the cathode, the existence of concentration gradients within the electrolyte have at least been subject of theoretical considerations. Especially the risk of electrolyte solidification due to compositional changes [38–42] has been discussed in this context.

Although barely studied in LMBs, it is well known from literature that composition gradients play an important role in molten salt electrolytes. Such phenomena have been widely investigated by Braunstein and Vallet in several publications [43–48] who show that concentration gradients in molten salts can be significant. The authors predicted concentration gradients in mixed cation molten salts based on equations that did not include convection terms [43, 44]. Later, these predictions were confirmed in several experiments with electrolytes contained in porous bodies that completely suppress or at least strongly damped any convective effects [46, 47]. These experiments were performed not only with low-melting model systems (such as NaCl-KCl-AlCl₃ or AgNO₃-NaNO₃ [46, 47]), but even with LMB-relevant LiCl-KCl [48]. The observed concentration gradients are caused by the electrode reactions, i.e. the electric current, as well as migrational and diffusive transport processes. This finally results in a depletion or enrichment of the electroactive species at the interfaces between electrodes and electrolyte [44, 45, 49]. The same authors show that current density, initial composition and differences in the mobility of the ions determine the final composition profiles [43].

Overall, the literature suggests that concentration gradients with possibly significant effects will appear not only in the cathode, but also in the electrolyte of LMBs. These will not only lead to concentration overpotentials [44], but might cause solidification [38–42, 44, 48], changes of the electric conductance, of the kinetics at the interfaces, increased corrosion [44] or a reduced energy utilisation [48]. Finally, if one interface completely depletes of the active species, undesired reactions might take place, such as the deposition of a previously passive species of the electrolyte [43].

Mass transport effects have, to a certain extent, been studied by numerical simulation – but almost exclusively within the cathode. Investigated phenomena include pure diffusion [3, 50], thermal convection [8, 51], solutal convection [52–55] and electro-vortex flow [11, 54, 56–58]. With the exception of one model [50, 56], the influence of the flow on the cell voltage has always been strongly simplified.

To the best knowledge of the authors, only Newhouse addressed mass transport in an LMB electrolyte theoretically [2]. Employing a one-dimensional model, she assumed a small concentration overpotential over the boundary layer in a very much simplified manner [2]. None of the previous studies regarded species transport or diffusive currents inside the electrolyte. Likewise, mass transport was up to now only simulated in the cathode. Hence, the present paper focuses on species transport in the electrolyte and investigates composition gradients which lead to concentration overpotentials in the electrolyte.

1.2. Modelling of liquid metal batteries

Many numerical studies regarding liquid metal batteries were performed by various authors. Thereby, the finite difference method (FDM) [3, 11, 59], the finite element method (FEM) [19, 57, 58, 60] and the finite volume method (FVM) [8, 10, 12, 14, 15, 21, 23, 25, 26, 50, 52, 53, 56, 61] were used. This indicates that the FVM is the most used method to investigate LMBs numerically. In general, FVM is the method of choice in computational fluid dynamics (CFD) whereas FEM is widely used in structural mechanics [62]. However, this does not mean that FDM and FEM are not suitable for such problems. Idelsohn and Oñate show that in particular cases and with wisely chosen discretisation procedures, the FVM and FEM can yield coincident results [63]. However, one of the main advantages of the FVM is that the conservative discretisation is automatically satisfied due to the mathematical formulation of the method, which makes it very attractive for the solution of convective dominant equations [62], like the Navier-Stokes equations. Contrarily, the FEM guarantees only global conservation and stabilising the discretisation for convection-dominated flow is not straightforward. So, additional computational effort is necessary and leads to higher computational cost for the fluid flow. For the FVM, computational times are lower [64]. A major drawback of the FVM becomes obvious, when it comes to the consideration of internal boundary values. Due to the cell-centred formulation, a solution on the boundary is not well defined. Boundary values need to be interpolated, which could potentially lead to problems in the present study, since the electrode-electrolyte interfaces need to be described at the boundaries of specific cells. This needs to be kept in mind for the development of a suitable numerical solver.

As the performance of LMBs is highly dependent on the fluid flow of the metals, the FVM is the method of choice. However, convection is not the only transport phenomenon that needs to be accounted for. If it is possible to simulate potential and species distribution in the whole cell accurately using the FVM, such a solver would be an ideal basis to investigate the impact of

various flow phenomena on the cell performance, which is the future goal for modelling LMBs.

For the development of a finite volume based solver for species transport and potential distribution in the Li||Bi cell, the single-potential approach that was introduced by Beale et al. [25, 65, 66] is used. Within this approach, one potential field is used for the whole battery. This couples the regions for anode, electrolyte and cathode using one matrix to obtain the electric potential in the whole domain. The remaining region-specific transport equations are solved on local meshes in a segregated manner and are iteratively coupled [65, 66].

When solving the electric potential, special care must be taken in describing the electrode-electrolyte interface, i.e. the electrical double layer (EDL). While microscopic models allow to completely resolve the EDL, certain macroscopic models simply replace it by a discrete “jump” in potential. The two jumps at the anode-electrolyte and electrolyte-cathode interfaces are then defined by the standard potential and represent the “driving force” of the battery current. In Fig. 2, a schematic illustration of the micro- and macroscopic approach, based on a model from Lueck and Latz [67], is shown.

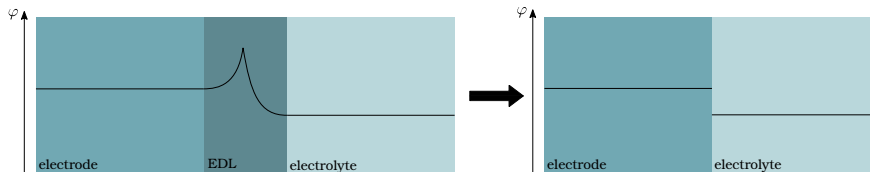


Figure 2: Schematic of an electrical double layer (left) and the simplification using a potential jump (right). Simplified adaption from [67].

Modelling a potential jump at an internal boundary within the FVM framework is generally possible by two different approaches. Firstly, it might be implemented as a volumetric source term in the Laplacian and gradient operator as done by Weber et al. [50]. Thus, an additional term appears, when grid cells that are touching the interface are involved.

An alternative approach for implementing the potential jump is the usage of cyclic (jump) boundary conditions [68–71]. Thereby, additional internal boundary conditions (BCs) are applied to infinitely thin interfaces between the different regions for electrodes and electrolyte. These BCs are periodic and hold an offset that is corresponding to the potential jump². The main advantage of this approach is that it largely relies on the standard OpenFOAM code and only requires slight changes to an existing boundary condition. For this reason, the present study employs this approach and considers interfacial jumps at anode-electrolyte and electrolyte-cathode interfaces without referring to measured or fitted values of the potential. No manipulation of the Laplacian and gradient operator is necessary and it is relatively easy to specify the regions and to iden-

²In OpenFOAM this BC is available as cyclic patch with a fixed jump [72].

tify and update the potential jump. Moreover, this is – to the best knowledge of the authors – the first study that investigates potential distributions in an LMB without resorting to fitted experimental data.

2. Mathematical and numerical model

2.1. Potential difference and overpotentials

The difference between both electrode potentials is the open circuit voltage (OCV) of the LMB [5]

$$E_{OC} = -\frac{RT}{zF} \ln a_{\text{Li(Bi)}} \quad (1)$$

with the universal gas constant R , the temperature T , z being the number of exchanged electrons, F the Faraday constant and a the activity of the active species (Li). When current flow is present, the available terminal voltage

$$E = E_{OC} - I \sum R - \eta_{c,a-e} - \eta_{c,e-c} - \eta_{c,c} - \eta_{a,a-e} - \eta_{a,e-c} \quad (2)$$

corresponds to the OCV being reduced by several voltage losses [73]. These overpotentials are outlined in Tab. 1 and are considered to have positive values. Mass transfer overpotentials η_{mt} result from inhomogeneous lithium distribu-

Table 1: Different types of overpotentials influencing the cell voltage of a battery.

symbol	description	group
$I \sum R = \eta_{\Omega}$	resistance overpotential	
$\eta_{c,a-e}$	concentration overpotential at anode-electrolyte interface	} η_{mt}
$\eta_{c,e-c}$	concentration overpotential at electrolyte-cathode interface	
$\eta_{c,c}$	concentration overpotential in the cathode	
$\eta_{a,a-e}$	activation overpotential at anode-electrolyte interface	} η_{ct}
$\eta_{a,e-c}$	activation overpotential at electrolyte-cathode interface	

tion, whereas resistance overpotential is mainly determined by the electrolytic resistance and can easily be calculated using Ohm’s law. The charge transfer overpotentials are primarily related to the electrode-electrolyte electron transfer, but their influence can be neglected since the exchange current densities for Li||Bi liquid metal batteries are high due to the high temperatures as well as rapid and facile charge-transfer reactions [28]. Ohmic losses are considered as the most dominant overpotentials in LMBs [5], nevertheless, the present study aims to quantify the influence of concentration overpotentials in cathode and

electrolyte on the cell performance.

The mass transfer overpotential in the whole cell can be obtained as [74]

$$\eta_{\text{mt}} = \frac{RT}{zF} \sum \nu_i \ln \frac{a_i}{\bar{a}_i} \quad (3)$$

being the sum of all mass transfer overpotentials with ν_i denoting the number of proton charges carried by an ion i , the volume-averaged activity \bar{a}_i and the activity of a species at the related interface a_i . Generally, such mass transfer overpotentials are a result of the current flow and the corresponding composition changes in the electrolyte [75]. Following Eq. (3), the concentration overpotential in the cathode can simply be calculated as [52, 74]

$$\eta_{\text{c,c}} = \left| \frac{RT}{zF} \left(\ln \frac{a_{\text{Li}}^{\text{c-e}}}{\bar{a}_{\text{Li(Bi)}}} \right) \right|. \quad (4)$$

At both electrolyte-electrode interfaces the following is deduced:

$$\begin{aligned} \eta_{\text{c,a-e}} &= \left| \frac{RT}{zF} \left(\nu_{\text{Li}^+} \ln \frac{a_{\text{Li}^+}^{\text{a-e}}}{\bar{a}_{\text{Li}^+}} \right) \right| \\ \eta_{\text{c,e-c}} &= \left| \frac{RT}{zF} \left(\nu_{\text{Li}^+} \ln \frac{a_{\text{Li}^+}^{\text{e-c}}}{\bar{a}_{\text{Li}^+}} \right) \right|. \end{aligned} \quad (5)$$

2.2. Problem description and simplifications

The present study investigates a simplified model of an LMB as it can be seen in Fig. 3a. Interfaces between the regions for anode, cathode and electrolyte are infinitesimally thin. Further, the figure shows the location where the overpotentials presented in Tab. 1 are located. For each region, different constants, parameters, initial fields, boundary conditions and physical properties are applied.

Figure 3b shows the simulation domain with corresponding patch names. The computational domain contains j cells. For better visualisation only a few specific cells are illustrated. Here, the bottom patch belongs to $j = 1$ and the top patch to $j = k$. The BC for the interfaces apply for both electrode-electrolyte interfaces; the owner cell of the jump BC is always located in the electrode, while the neighbour cell is located in the electrolyte. Simulations are done “quasi” one-dimensional using the FVM with the model being implemented in the open-source library OpenFOAM [76]. Moreover the following simplifications are made:

- All convective and thermal effects³ are neglected,
- activation overpotentials are not taken into account,

³Fluid flow, heat transfer, Joule heating and volume change.

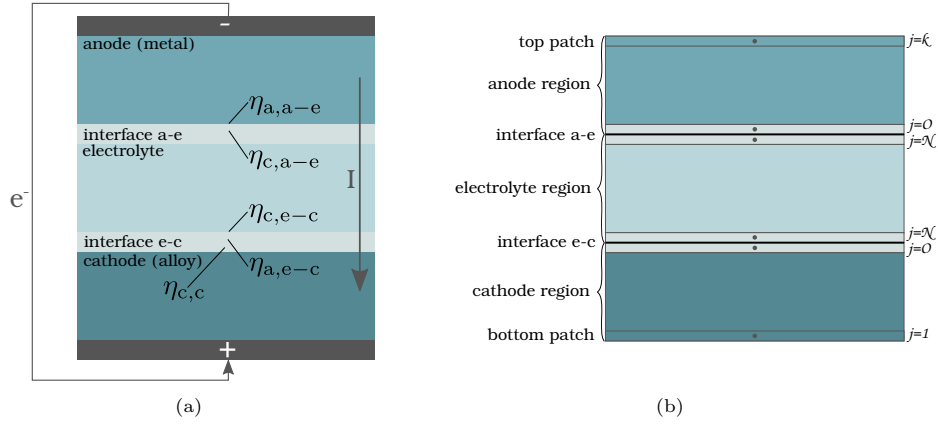


Figure 3: Simulation (a) setup and (b) domain.

- the electrolyte is assumed to have ideal ionic behaviour,
- the current collectors are not modelled,
- and diffusion coefficients as well as activity coefficients are calculated based on additional assumptions due to the lack of exact values.

These simplifications allow to investigate mass transport in the electrolyte fundamentally. By neglecting fluid flow, the maximal possible diffusion loss may be quantified and be compared with ohmic losses. While the results are directly valid for those batteries, where the electrolyte has been soaked into an inert filler material [73, 77], convection might be important for fully liquid cells [5]. The latter aspect is briefly discussed at the end of section 5.

2.3. Transport equations and boundary conditions

In this section, the electrochemical equations for molten electrodes and electrolytes are presented. They follow Newman [75], if nothing else is mentioned. There are two transport equations that will be discussed: first, the transport of charge and second, the transport of species. Equations in section 2.3.1 are relevant for the whole computational domain, while those in section 2.3.2 and 2.3.3 are solved on the electrolyte or cathode sub-grid.

2.3.1. Entire battery

When a potential difference is applied to an electric conductor, electrons start to flow due to the gradient in potential φ . The current density \mathbf{j} is related to the flow of electrons and can be calculated using Ohm's law

$$\mathbf{j} = -\sigma \nabla \varphi \quad (6)$$

with the electric conductivity σ . Taking the conservation of charge

$$\nabla \cdot \mathbf{j} = 0 \quad (7)$$

into account, this leads to the Laplace equation for the potential distribution

$$\nabla \cdot (\sigma \nabla \varphi) = 0. \quad (8)$$

For calculating the potential, the global mesh is used. Under galvanostatic control, a Neumann BC

$$\sigma_k \left. \frac{\partial \varphi_k}{\partial \mathbf{n}} \right|_f = \frac{I}{A_{f,k}} \quad (9)$$

for the top patch is used, where $n = k$. Here, \mathbf{n} denotes the normal face vector at the face f and the associated area A . At the bottom patch, a Dirichlet BC

$$\varphi_1|_f = \text{const.} = 0 \quad (10)$$

with $k = 1$ applies.

2.3.2. Electrolyte

When solving species conservation within the electrolyte layer, the Laplace equation needs to be substituted by a Poisson equation in the following manner. In the electrolyte the current represents the net flux of the charged species and the current density is defined as

$$\mathbf{j} = F \sum_{i=1}^n \nu_i \mathbf{N}_i, \quad (11)$$

with the flux density of each species \mathbf{N}_i . The latter is expressed by the Nernst-Planck equation

$$\mathbf{N}_i = \underbrace{-\nu_i \mu_i F c_i \nabla \varphi}_{\text{migration}} - \underbrace{D_i \nabla c_i}_{\text{diffusion}} + \underbrace{c_i \mathbf{u}}_{\text{convection}} \quad (12)$$

with the concentration c_i , the mobility μ_i and the diffusion coefficient D_i of a species as well as the velocity \mathbf{u} . The Nernst-Einstein relation

$$\mu_i = \frac{D_i}{RT} \quad (13)$$

is used to calculate the mobility of a species. Further, a material balance for each species

$$\underbrace{\frac{\partial c_i}{\partial t}}_{\text{accumulation}} = \underbrace{-\nabla \cdot \mathbf{N}_i}_{\text{net input}} + \underbrace{R_i}_{\text{production}} \quad (14)$$

with the production R_i can be derived. Finally, the condition of electroneutrality

$$\sum_i \nu_i c_i = 0 \quad (15)$$

applies for electrolytic solutions. Equations (11), (12), (14) and (15) describe the transport processes in electrolytic solutions. In the present study $R_i = 0$

and $\mathbf{u} = 0$. When combining Eq. (11) and Eq. (12), it can be seen that the current density

$$\mathbf{j} = -F^2 \nabla \varphi \sum_i \nu_i^2 \mu_i c_i - F \sum_i \nu_i D_i \nabla c_i \quad (16)$$

can be divided into two parts as well. The first term describes the migrational current density \mathbf{j}_m and the second the diffusive current density \mathbf{j}_d . Since the current due to migration is closely related to the flow of electrons, the electric conductivity in the salt can be written as

$$\sigma_{\text{salt}} = F^2 \sum_i \nu_i^2 \mu_i c_i, \quad (17)$$

which finally yields

$$\begin{aligned} \mathbf{j} &= -\sigma \nabla \varphi - F \sum_i \nu_i D_i \nabla c_i \\ &= \mathbf{j}_m + \mathbf{j}_d. \end{aligned} \quad (18)$$

Taking conservation of charge into account leads to the Poisson equation

$$\nabla \cdot (\sigma \nabla \varphi) = \nabla \cdot \left(-F \sum_i \nu_i D_i \nabla c_i \right) \quad (19)$$

for calculating the potential distribution in an electrolyte.

From the equations in section 2.3.2, it can be concluded that the potential distribution inside the whole liquid metal battery can be calculated using only the Poisson equation (19). The source term on the right-hand side (RHS) of Eq. (19) is zero in the electrodes. Since the present study solves the potential jump at the interfaces between electrode and electrolyte as well, the meshes of electrolyte and electrode can be coupled. Solving the potential distribution on a global mesh respects both, the potential jumps as internal jumps and the different regions in the battery. The potential jumps are addressed in section 2.4 in more detail.

Further, the species – or mass – transport can be derived by combining Eq. (12) and Eq. (14). This leads to

$$\frac{\partial c_i}{\partial t} = \nu_i \mu_i F \nabla \cdot (c_i \nabla \varphi) + \nabla \cdot (D_i \nabla c_i) \quad (20)$$

which describes the transport of each species. At all boundaries not belonging to an electrolyte-electrode interface, zero flux boundary conditions apply.

For the electrolyte, a general case with more than two species and one active species is regarded. Therefore, each species must be classified as active or passive. Only active species – here lithium cations – take part in the electrode-reactions. To derive their BCs, Eq. (12) is reordered leading to an expression for the potential gradient. Multiplying with ν_i/D_i , summing up over all species and using the Nernst-Einstein relation (Eq. (13)) gives

$$\nabla \varphi = - \frac{RT \sum_i \mathbf{N}_i \frac{\nu_i}{D_i}}{F \sum_i \nu_i^2 c_i}. \quad (21)$$

Together with Eq. (16), the following can be derived for an arbitrary species j :

$$\nabla c_j = \frac{-\mathbf{N}_j + \nu_j D_j c_j \frac{\sum_i \mathbf{N}_i \frac{\nu_i}{D_i}}{\sum_i \nu_i^2 c_i}}{D_j}. \quad (22)$$

For a species j , the current density can be calculated as $\mathbf{j} = F\nu_j \mathbf{N}_j$ using Eq. (11). The term $\sum_i \mathbf{N}_i \frac{\nu_i}{D_i}$ must include only active species, since no passive species flows across the boundaries. To differentiate between active (index 1) and passive (index p) species, two boundary conditions are needed. Firstly, for the active species

$$\nabla c_1 = \frac{\mathbf{j}}{F\nu_1 D_1} \left(\frac{\nu_1^2 c_1}{\sum_i \nu_i^2 c_i} - 1 \right) \quad (23)$$

can be found. Secondly, for the passive species

$$\nabla c_p = \frac{\mathbf{j}}{F\nu_1 D_1} \frac{\nu_1 \nu_p c_p}{\sum_i \nu_i^2 c_i} \quad (24)$$

is valid. Since the condition of electroneutrality (Eq. (15)) must be fulfilled, the species transport needs to be solved for $n - 1$ species only. The concentration distribution for species n is calculated from electroneutrality.

The species transport is solved on the local mesh for the electrolyte region, using the mapped current density. Here, both interfaces are treated with Neumann BCs according to the derived conditions for active (Eq. (23)) and passive species (Eq. (24)).

2.3.3. Cathode

At discharge, lithium dissolves into the bismuth cathode. There, no migration occurs since no charged species is present. Therefore, the transport equation for the molar concentration respectively lithium distribution reads

$$\frac{\partial c}{\partial t} = \nabla \cdot (D \nabla c). \quad (25)$$

For the boundary condition of the lithium concentration at the cathode interface, the derivation is quite straightforward. Equation (11) reduces to $\mathbf{j} = Fz\mathbf{N}$, since there is only a flux of lithium. Together with Eq. (25) the boundary condition is

$$\nabla c = -\frac{\mathbf{j}}{FzD}. \quad (26)$$

To solve the lithium distribution in the cathode, a zero gradient Neumann BC is applied at the bottom patch.

2.4. Potential jump

Instead of resolving the EDL numerically, the electrode potential of each half-cell can be expressed – on a macroscopic scale – as a potential jump between electrode and electrolyte. In the following it is shown how this is done in

particular.

The Li||Bi liquid metal battery is a concentration cell and the electrode reaction at the anode



and at the cathode



occur due to the material paring Li||Bi. So, the potential jumps at the anode-electrolyte interface and the electrolyte-cathode interface are in accordance to the Nernst-Equation

$$\varphi = \varphi_0 + \frac{RT}{zF} \ln \frac{a_{\text{ox}}}{a_{\text{red}}} \quad (29)$$

with the standard potential φ_0 and the activity of the reduced and oxidised species a . For a Li||Bi LMB, the number of exchanged electrons is $z = 1$.

Since concentration cells are made out of two half cells, the potential jumps at the anode and cathode are the following:

$$\Delta\varphi_{\text{a-e}} = \varphi_0 + \frac{RT}{zF} \ln \frac{a_{\text{Li}^+}}{a_{\text{Li}}}, \quad (30)$$

$$\Delta\varphi_{\text{e-c}} = \varphi_0 + \frac{RT}{zF} \ln \frac{a_{\text{Li}^+}}{a_{\text{Li}(\text{Bi})}}. \quad (31)$$

The activity of pure lithium is $a_{\text{Li}} = 1$; for the other values, see section 2.5.

In OpenFOAM, the potential jump can be modelled using a jump cyclic boundary condition [71, 78]. The basis for this is the predefined fixedJump BC which is slightly modified by the authors of the present study, so that the jump can be updated in every time step. Mathematically the potential jump over an interface f is expressed as

$$\varphi_{\text{N}}|_f = \varphi_{\text{O}}|_f - \Delta\varphi, \quad (32)$$

where O refers the owner and N to the neighbour cell as it was shown in Fig. 3a. The OCV of the battery (see Eq. (1)) is the difference between the two potentials of the electrodes $E_{\text{OC}} = \varphi_{\text{c}} - \varphi_{\text{a}}$. Figure 4 shows a schematic sketch of the potential profile in the battery. Here, the potential jump $\Delta\varphi$ at both interfaces indicated by Eq. (32) can be seen as well. In a global manner, the potential gradient in the cell needs to be negative since for discharge, the potential of the anode must be smaller than the one of the cathode. For the specific regions, the potential gradient is positive as it is indicated by Eq. (6).

2.5. Material properties

To compute the initial Li concentration in Bi, the density of the Li(Bi) alloy in the cathode is required. The latter is obtained (in kg/m³) as an empirical formula which is based on values from Wax et al. [79] and Steinleitner et al. [80] as

$$\rho = -7357x^2 - 2045x + 9863 \quad (33)$$

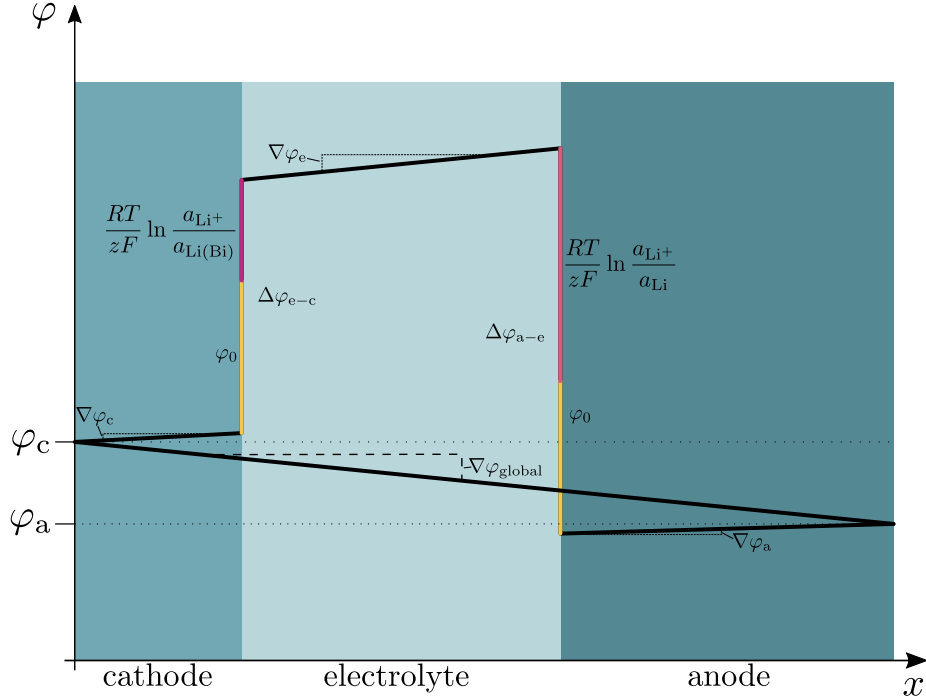


Figure 4: Relation between open circuit voltage and potential jumps without consideration of the overpotentials.

with x denoting the molar fraction of Li in Bi. For alternative density functions, see [3]. Subsequently, the concentration of lithium can be computed as

$$c = \frac{x\rho}{xM_{\text{Li}} + (1-x)M_{\text{Bi}}}. \quad (34)$$

The molar concentrations of the different species in the electrolyte can be calculated as

$$c_i = \chi_i c_{\text{salt}} \quad (35)$$

with χ being the molar fraction of the species in the electrolyte. To calculate the total concentration of the electrolyte

$$c_{\text{salt}} = \frac{\rho_{\text{salt}}}{M_{\text{salt}}} \quad (36)$$

the molar mass

$$M_{\text{salt}} = \sum \chi_i M_i \quad (37)$$

needs to be calculated using the electrolyte composition, where the subscript i refers to the salt components and not to the single species. Here, eutectic LiCl-KCl (58.8:41.2 mol%) is considered.

The electric conductivity of the electrolyte can be used to estimate the diffusivity

of the species. Morgan and Madden [81] investigated the diffusion coefficients of the species in the here concerned molten salt for some temperatures and in dependence of the molar fraction of the potassium ion χ_{K^+} . For the present $\chi_{K^+} = 0.206$, it is found that $D_{Li^+} > D_{K^+} > D_{Cl^-}$. To adapt the diffusion coefficients to a specific temperature, ratios between the D_i obtained by Morgan and Madden [81] at $T = 900K$, were derived. It is found that

$$\begin{aligned} A &= \frac{D_{Cl^-}}{D_{Li^+}} = 0.807 \\ B &= \frac{D_{K^+}}{D_{Li^+}} = 0.895. \end{aligned} \quad (38)$$

Applying the relations above to Eq. (17) with using Eq. (13), the diffusion coefficient for lithium in LiCl-KCl (eutectic)

$$D_{Li^+} = \frac{\sigma_{salt} RT}{F^2 (c_{Li^+} + A c_{Cl^-} + B c_{K^+})} \quad (39)$$

can be derived. Ionic diffusion coefficients for the other species follow from the relations in Eq. (38).

Another important property is the activity of Li in Bi and the activity of the various ions in the molten salt. The latter are of interest for the calculation of the Nernst equation (29) and the potential jump at the interfaces between electrolyte and electrodes. As the present study aims to develop and demonstrate the electrochemical model in its simplest form, the activity of Li in Bi is assumed not to deviate from ideality and is described as

$$a_{Li(Bi)} = x_{Li(Bi)}. \quad (40)$$

For an overview on realistic activities of Li in Bi, see [3].

Unfortunately, values for activities of molten salts are often only approximately known and determinable [82, 83]. Therefore, the ionic activities of Li^+ , K^+ and Cl^- are estimated using Temkin's model as [84, 85]

$$a_i = \chi_i \quad (41)$$

again assuming the activity coefficient to be unity. Please note that χ_i describes here the mole fraction of an ion related to all ions of the same charge. So, in terms of determining the activity of a salt, separate solutions of cations and anions are considered.

The values used for the simulation will be explicitly given in section 4.1.1.

3. Numerical implementation

3.1. Modified species transport equation

In our model, special care needs to be taken in expressing the migrational flux when solving the species transport equation (20). As explained in detail

in [Appendix A](#), limitations in the gradient calculation of the potential require rewriting the migrational term. Thus, Eq. (20) is reformulated as

$$\frac{\partial c_i}{\partial t} = \nabla \cdot (\Psi c_i) + \nabla \cdot (D_i \nabla c_i) \quad (42)$$

with

$$\Psi = \nu_i \mu_i F \nabla \varphi. \quad (43)$$

Reordering Eq. (18) gives

$$\Psi = -\nu_i \mu_i F \left(\frac{\mathbf{j} + F \sum_i \nu_i D_i \nabla c_i}{\sigma} \right), \quad (44)$$

so that the electric potential is not required any more for solving the species transport. This formulation is necessary to avoid the generation of divergence near the electrode-electrolyte interface.

3.2. Mesh coupling and simulation routine

The computational domain consists of three regions for anode, electrolyte and cathode. Since the electric current passes all three regions, a classical segregated solver with potential coupling only at the interfaces using boundary conditions is not suitable and shows poor convergence [25]. Facing this problem, Weber et al. introduced a parent-child mesh technique for calculating the potential distribution in a liquid metal battery. For that matter, global variables are solved on a global (parent) mesh and local (child) meshes for specific regions are used to solve local variables. Before, this approach has already been used for calculations of thermal conduction [65, 66] and eddy-current problems [86].

The latter matches with the parent-child-mesh technique used in the present study. Field variables and region properties can be mapped between the different meshes and they share common values. Globally, the boundaries between the regions are internal boundaries, while locally, the boundaries are external. This allows more flexibility and better computational efficiency while more detailed simulations can be performed.

In the present study the electric potential and current density are solved on the global mesh. Further, there is a mesh for each electrode and one for the electrolyte. The anode is not of special interest, so there are no additional transport equations solved. In the cathode, the concentration of lithium in bismuth is calculated. Whereas, in the electrolyte the corresponding electric conductivity, the species distribution and the diffusive current density are computed. Here, it is important to consider that the electric conductivity is different in each region. This will further be discussed in section 3.3.

In Fig. 5, the scheme of the simulation model is shown. It can be seen that the electric conductivity σ and the current density \mathbf{j} are the variables of interest for mapping. As an overview, Tab. 2 shows the equations solved in the different regions. All of them are solved in a segregated manner and are iteratively coupled.

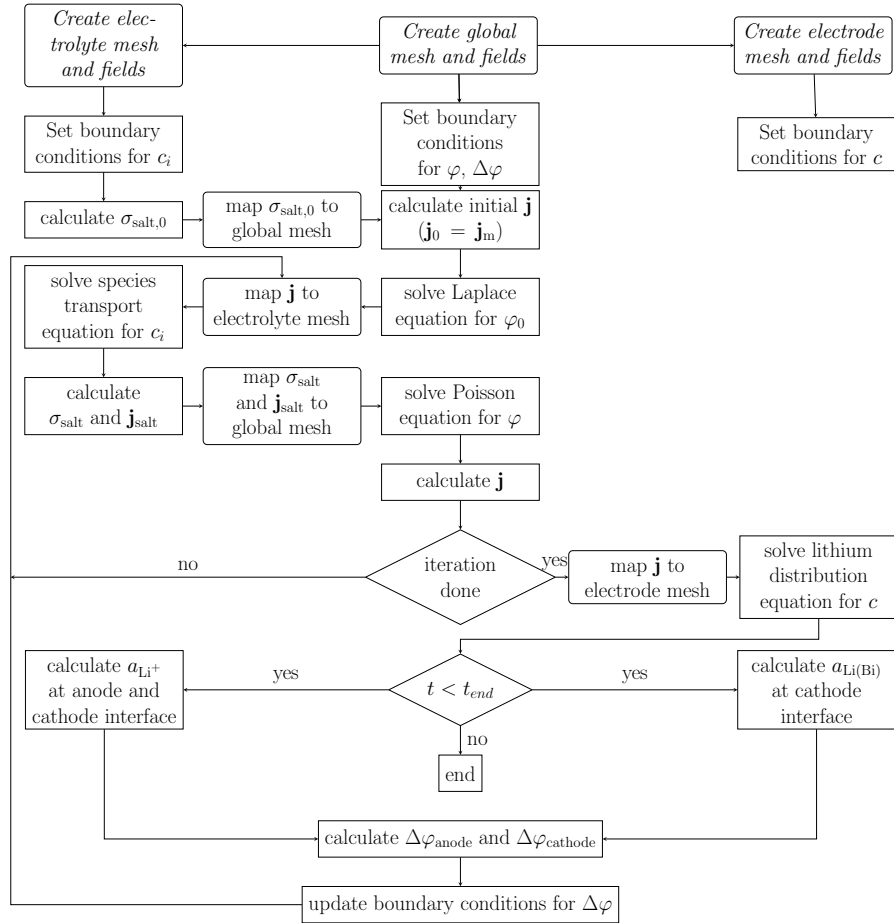


Figure 5: Flowchart of the simulation model.

Table 2: Meshes and the related equations.

mesh	equations
global	Eq. (19) and Eq. (18)
electrolyte	Eq. (42) using Eq. (44)
cathode	Eq. (25)

Further, continuity of the current density ensures sufficient region and mesh coupling. Numerically, this requires continuity at the cell faces – especially at those cells connecting two regions. The potential jump has a similar importance. Both leads to the consequence that special discretisation in the interface region is required. This will be elaborated in the following sections.

3.3. Discretisation

The potential jump and the multi-mesh approach require special attention for the discretisation of some terms in the solved equations. Especially the Poisson equation (Eq. (19)) needs to be considered.

Equation (25) for calculating the lithium distribution in the cathode and Eq. (42) for the species transport in the electrolyte do not need special treatment. Here, a first order Euler implicit scheme for the time discretisation, a second order linear scheme for the Laplacian and an upwind differencing interpolation scheme for the divergence term are used. Due to the different regions with highly differing electric conductivities, sharp jumps at the interfaces are present. As continuity at the cell faces is required, the face values for the potential and the conductivity are needed. In the FVM, cell values are interpolated to the faces. To avoid wrong potential calculations due to inconsistency caused by numerical errors, the electric conductivity must be interpolated harmonically. This can be expressed as

$$\sigma_f = \left(\frac{\delta_O}{\delta\sigma_O} + \frac{\delta_N}{\delta\sigma_N} \right)^{-1} \quad (45)$$

with δ_O and δ_N being the distance from cell centre to cell face of owner respectively neighbour cell and the distance between both cell centres δ [25, 86, 87]. Moreover, care must be taken when discretising Eq. (18) and Eq. (19) since they include σ . First, the current density calculation is described. OpenFOAM uses the Gauss theorem [72] to compute the gradient

$$\int_V \nabla\varphi dV = \int_S d\mathbf{S}\varphi = \sum_f \mathbf{S}_f\varphi_f \quad (46)$$

with the volume V and the surface area S of a cell, the surface area vector \mathbf{S} and the face area vector \mathbf{S}_f . So, the face values of the potential are needed. Following this, the potential gradient is discretised using the weightedFlux scheme, which is derived in a similar way as harmonic interpolation as in [25]

$$\varphi_f = w\varphi_O + (1 - w)\varphi_N \quad (47)$$

with

$$w = \frac{\delta_N \sigma_O}{\delta_O \sigma_N + \delta_N \sigma_O}, \quad (48)$$

which gives accurate solutions for the migrational current density.

Solving Eq. (19) for the electric potential, a consistent discretisation like in the balanced-force approach [88, 89] is employed to guarantee numerical accuracy. This idea is applied to the present model, which means that the left-hand side (LHS) and RHS of the Poisson equation (19) need to be in exact balance to calculate the potential jump correctly. The LHS is discretised using a harmonic Laplacian scheme

$$\int_V \nabla \cdot (\sigma \nabla \varphi) dV = \int_S d\mathbf{S} \cdot (\sigma \nabla \varphi) = \sum_f \sigma_f \mathbf{S}_f \cdot \nabla (\varphi)_f. \quad (49)$$

It can be seen that the potential gradient is calculated at the cell faces. The RHS is discretised as

$$\int_V \nabla \cdot \mathbf{j}_d dV = \int_S d\mathbf{S} \cdot \mathbf{j}_d = \sum_f \mathbf{S}_f \cdot (\mathbf{j}_d)_f. \quad (50)$$

Here, the face values of the diffusive current density $(\mathbf{j}_d)_f$ are needed. To avoid inaccurate face values, interpolation from cell to face must be avoided. Instead, the face value $(\mathbf{j}_d)_f$ is calculated directly from the face values of the concentration gradient $\nabla(c_i)_f$:

$$\sum_f \mathbf{S}_f \cdot (\mathbf{j}_d)_f = \sum_f \mathbf{S}_f \cdot \left(-F \sum \nu_i D_i (\nabla c_i)_f \right). \quad (51)$$

This is accurate, since $(\nabla c_i)_f$ is implemented as BC. Using the procedure above, $\mathbf{j} = \mathbf{j}_m + \mathbf{j}_d$ (Eq. (18)) is continuous over the computational domain.

4. Verification and validation

To verify the numerical solver, a comparative study with the commercial FEM solver COMSOL Multiphysics is performed. Detailed results can be found in [Supplementary material S1](#). Experimental investigations of the composition gradients in LiCl-KCl from Vallet et al. [48] are further taken into consideration for the validation of the presented numerical solver.

4.1. Simulation results for comparison OpenFOAM-COMSOL

4.1.1. Simulation parameters

In the following, a Li|LiCl-KCl|Bi liquid metal battery at $T = 450^\circ\text{C}$ is considered. The LiCl-KCl electrolyte is an eutectic mixture (58.8:41.2 mol%) and can be classified as salt system of three ions – in the present study the electrolyte is therefore named “ternary”. The geometry of the battery is simplified

according to Fig. 3a, but numerically considered to be one-dimensional. The height of the anode is $h_a = 16\text{mm}$, of the electrolyte $h_e = 5\text{mm}$ and of the cathode $h_c = 4\text{mm}$. The anode-electrolyte interface is located at $x = 9\text{mm}$ and the electrolyte-cathode interface at $x = 4\text{mm}$. A discharge current density of $\mathbf{j} = -100\text{mA/cm}^2$ and a time of $t = 600\text{s}$ are chosen. Molar mass, density and electric conductivity for the electrodes and the electrolyte are shown in Tab. 3.

Estimating the initial concentration of the species and their diffusion coef-

Table 3: Material properties at 450°C [90–92].

Property	Li	Bi	LiCl-KCl
M in g/mol	6.94	208.98	55.64
ρ in kg/m^3	491	9839	1671
σ in S/m	$2.78 \cdot 10^6$	$7.14 \cdot 10^5$	157.28

ficients in the electrolyte is done in accordance with the equations stated in section 2.5. The initial concentration of the electrolyte is $c_{\text{salt}} = 30\,028\text{ mol/m}^3$. Using the molar fractions of each species, the concentrations for each ion can be calculated as shown in Tab. 4. The diffusion coefficients follow from Eq. (39) and Eq. (38). The diffusivity of lithium in bismuth is calculated according to Newhouse [2]:

$$D_{\text{Li(Bi)}} = \exp \frac{-4.081c_{\text{Li}} - 0.01315}{c_{\text{Li}}^2 + 0.3742c_{\text{Li}} + 0.001572} \quad (52)$$

with c denoting the molar concentration of Li in Bi in mol/cm^3 . The initial

Table 4: Initial concentrations.

Species	Li(Bi)	Li^+	Cl^-	K^+
z / ν	1	1	-1	1
c in mol/m^3	13125	8828	15014	6186
D in m^2/s	$4.43 \cdot 10^{-9}$	$3.84 \cdot 10^{-9}$	$3.1 \cdot 10^{-9}$	$3.43 \cdot 10^{-9}$

concentration of lithium in bismuth can be derived from Eq. (33) and (34). Here, an arbitrary initial state of charge with an initial molar fraction of lithium $x_0 = 0.236$ is chosen.

To verify the presented solver, obtain deeper and piecewise detailed results as well as to investigate the influence of individual parameters on the cell performance, four test cases of different complexity are used:

1. binary electrolyte (LiCl), equal diffusion coefficients, potential jump is not modelled
2. binary electrolyte (LiCl), potential jump is not modelled
3. ternary electrolyte (LiCl-KCl), potential jump is not modelled
4. ternary electrolyte (LiCl-KCl), fixed potential jump is modelled

Here, “binary” refers to a salt with two ions. Although the test cases are purely fictive, the values in Tab. 3 are used. For test case 1 it is assumed that $D_{\text{Cl}^-} = D_{\text{Li}^+} = 3.84 \cdot 10^{-9} \text{ m}^2/\text{s}$ and $c_{\text{Li}^+} = c_{\text{Cl}^-} = 13239 \text{ mol}/\text{m}^3$, while for test case 2 $c_{\text{Li}^+} = c_{\text{Cl}^-} = 14654 \text{ mol}/\text{m}^3$ is used. The potential jumps in test case 4 are arbitrarily chosen as $\Delta\varphi_{\text{a-e}} = 0.8\text{V}$ and $\Delta\varphi_{\text{e-c}} = 1\text{V}$. In all simulations, the active species lithium is calculated from electroneutrality. An additional grid study and electroneutrality study can be found in [Supplementary material S2](#) and [Supplementary material S3](#).

For each simulation, the species concentration in the electrolyte and the potential distribution in the whole cell are compared between COMSOL multi-physics and OpenFOAM to verify the latter. Only main findings are presented here, additional information and figures can be found in [Supplementary material S1](#). In general, the results – even if only presented in supplementary material – of the OpenFOAM simulations highly coincide with the results obtained using COMSOL. The former can therefore be considered to be verified.

4.1.2. Test cases

Test case 1 is the most simple one as it is highlighted in [Appendix A](#). In the absence of concentration gradients in the electrolyte, the current can be determined by migration only and Eq. (18) reduces to Eq. (6) which describes the current density in the electrodes as well. Here, no diffusive current is flowing and only the Laplace equation for the potential distribution Eq. (8) needs to be solved. Analytically calculating the diffusive current density of the lithium ion from the concentration gradient for the initial state using Eq. (23) and Eq. (18) gives $j_{\text{d,Li}^+}^{t_0} = 500 \text{ A}/\text{m}^2$ which fits with the results obtained by the OpenFOAM simulation. Further, the electric losses in the electrolyte are almost constant over time.

Not assuming equal diffusion coefficients in test case 2 makes it necessary to solve the Poisson equation for the potential distribution, Eq. (19). Thus, the diffusive part of the current density has now an impact on the solution: it influences the electric losses significantly, which indicates that the overall ohmic loss in the electrolyte is determined not only by electric conductivity, but also by the diffusive current. The latter – or diffusion itself – contributes to charge transport without causing ohmic losses. In the present case, the electric loss decreases over time about approx. 6% during the whole simulation, so a better cell performance due to increasing diffusive current could be expected. Similarly, the diffusive current density is approx. 6% of the current density on average at the end of the simulation (cf. Fig. S1.15). A clear coincidence can be seen here. In contrast, unequal diffusion coefficients have no impact on the species distribution as long as only two species are involved⁴.

Now, a closer look to the species distribution is necessary since a ternary electrolyte is considered in test case 3. Calculating the initial diffusive current density for each ion using Eq. (23), Eq. (24) and Eq. (18) gives $j_{\text{d,Li}^+}^{t_0} = 706$

⁴The values of the concentration gradients for test case 1 and 2 are coincident.

A/m², $j_{d,\text{Cl}^-}^{t_0} = 404 \text{ A/m}^2$ and $j_{d,\text{K}^+}^{t_0} = -184 \text{ A/m}^2$. In the simulations those values are obtained as well as it is shown in Fig. S1.16. As it can be seen in Fig. 6, more LiCl is accumulated at the anode while more KCl is accumulated at the cathode interface and vice versa. Compared with experimental work, the presented results are in qualitative good agreement with the results from Vallet et al. [48] who determined composition gradients in LiCl-KCl.

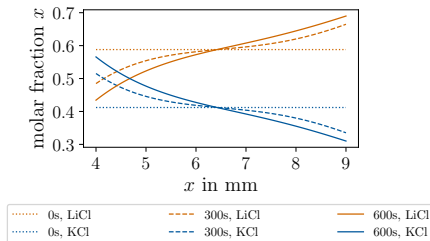


Figure 6: Test case 3; results for OpenFOAM simulation: species distribution of LiCl and KCl expressed in molar fraction.

In order to approach the verification test cases closer to real conditions in a cell, two potential jumps are added at the electrolyte-electrode interfaces in test case 4. Everything else is taken from test case 3. The potential jumps $\Delta\varphi_{a-e}$ and $\Delta\varphi_{e-c}$ always refer to a viewpoint from electrolyte to electrode. Here again, the potential at the anode decreases over time, which agrees with the previous observations: the electric resistance declines due to the diffusive current being lossless in terms of charge transfer.

4.2. Comparison with experiment

After the verification with COMSOL, the solver is validated using experimental data. Vallet et al. electrolysed eutectic LiCl-KCl contained in porous yttria felt at 425°C [48]. The cell consisted of a 4.16 mm thick electrolyte between two solid Li-Al electrodes and was operated for 242 s at 254 mA/cm². After electrolysis, the sample was cooled down to room temperature in less than one second to analyse its composition. Atomic absorption spectroscopy (AAS) with a lateral resolution of 0.4 mm and an accuracy of approximately 6% was used together with energy-dispersive X-ray spectroscopy (EDX) to obtain the KCl molar fraction. Several EDX scans with an accuracy of 8% in a slice of less than 0.18 mm were averaged to obtain a single point. Finally, the data was fitted by an empirical formula.

Modelling this experiment, the same material properties as in section 4.1.1 are used. The effective diffusion coefficients in the yttria matrix are obtained as

$$D_{\text{eff},i} = \frac{D_i}{\tau^2} \quad (53)$$

with the tortuosity τ . As the latter had not been measured for the felt under consideration, a value of $\tau = 1.17$ for a similar yttria matrix is used [47]. The felt reduces the diffusivities by almost 30%.

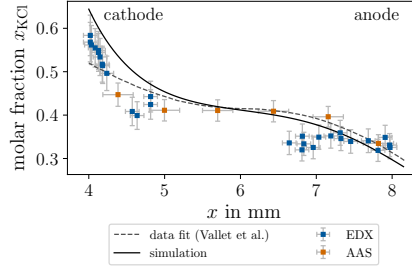


Figure 7: Distribution of KCl in cell No. 2 of Vallet et al. [48].

Fig. 7 shows the numerical and experimental results, which match fairly well. The remaining deviations can be attributed to a number of different sources, such as imperfect wetting of the yttria matrix by the salt, an inhomogeneous yttria felt and current density [48], measurement errors of EDX and AAS of up to 10%, back-diffusion during cooling and the not exactly known tortuosity. As the latter was measured for a felt with a porosity of 90% instead of $85 \pm 4\%$ as in this experiment, the effective diffusion coefficients might in reality be lower. The largest uncertainty comes, however, from the diffusion coefficient itself. Available measurement data is very scarce and might contain considerable error. Further, the diffusivity is expected to depend on concentration [2]. Tab. 5 gives an overview of diffusion coefficients in LiCl-KCl available in literature. Taking into account that even for similar temperatures the values vary up to a factor of six, the observed deviation between experiment and simulation appears to be acceptable.

Table 5: Various diffusion coefficients for Li^+ , Cl^- and K^+ in LiCl-KCl molten salt.

D_i in 10^{-9} m ² /s			T in °C	Source	
Li^+	Cl^-	K^+			
1.0	1.0	1.0	425	estimate	[43, 44]
0.7	1.2	1.1	367	molecular dynamics	[93]
2.02	1.75	2.25	373	molecular dynamics	[94]
1.0		1.0	450	estimate	[95]
2.6		2.8	430	measured ¹	[96]
6.2	6.1	6.2	757	molecular dynamics	[97]
5.7	4.6	5.1	627	molecular dynamics	[81]
0.668			450	measured	[98]
4.37	3.7	4.89	527	molecular dynamics	[99]
10.0		10.0	827	molecular dynamics	[100]
2.4	1.2	2.0	450	no reference	[101]
3.8	3.1	3.4	425	present work	

5. Application to a Li||Bi battery and discussion

In this section, the previously derived solver is used to investigate the overpotentials introduced in section 2.1 in a Li|LiCl-KCl|Bi cell. Dimensions and material properties are in accordance to those described before in section 4.1.1. Moreover, the potential jumps will be calculated in every time step based on the Nernst equation (Eq. (30) & Eq.(31)) as well as the corresponding activities at the electrode-electrolyte interfaces.

Investigations were done with different current densities. In order to identify a working range of the cell, it is important to know the limiting current density j_{lim} . For the LiCl-KCl electrolyte the diffusive limiting current density reads

$$j_{\text{lim,d}} = -zF\frac{\bar{c}}{\delta}D \quad (54)$$

with δ being the maximum thickness of the diffusion layer. In steady state and neglecting convection, the latter can be approximated as the half electrolyte thickness [74]. In the present application case $j_{\text{lim}} \approx -130\text{mA}/\text{cm}^2$. Nevertheless, comparative simulations are performed with $j_1 = -100\text{mA}/\text{cm}^2$, $j_2 = -150\text{mA}/\text{cm}^2$, $j_3 = -200\text{mA}/\text{cm}^2$ and $j_4 = -250\text{mA}/\text{cm}^2$.

In the following, the potential in the entire cell and species distribution in electrolyte and cathode are analysed. Specifically, (i) the terminal voltage of the battery (ii) the OCV and (iii) the different overpotentials giving information about the composition of the cell voltage will be studied. This makes it possible to compare the simulations with the theoretical principles. Further, it is analysed how the ratio of concentration overpotentials to ohmic overpotential for different current densities develops. Lastly, a polarisation curve is drawn for the applied current density range between 0 and $-250\text{mA}/\text{cm}^2$.

Before showing comparative results, some outcomes of the simulation for j_1 are presented. The distribution of LiCl and KCl in the electrolyte (see Fig. 8a) shows the same behaviour as in the verification study in section 4.1. In contrast to the previous simulations, the lithium distribution in the bismuth cathode, as it can be seen in Fig. 8b, is modelled and analysed now as well. Arriving from the electrolyte, the Li diffuses into the cathode and accumulates at the interface. For the cell voltage, the distribution of lithium in bismuth has a decisive impact. It can be seen in Eq. (1) that the corresponding activity determines the cell voltage and is significantly involved in the potential jump at the cathode.

Now, a closer look to the composition of the overvoltages according to Eq. (2) is taken. The results are shown in Fig. 9a. There, the theoretical open circuit voltage is calculated from the activity of Li(Bi) (Eq. (40)), while the terminal voltage is a direct outcome of the simulation. Both are coloured in blue. Here it is apparent that the cell voltage of the Li||Bi cell is much lower, than the value known from pertinent literature [73, 77, 102]. For the used Li||Bi cell an

¹Measured mobilities have been used to compute the diffusion coefficients via the Nernst-Einstein relation.

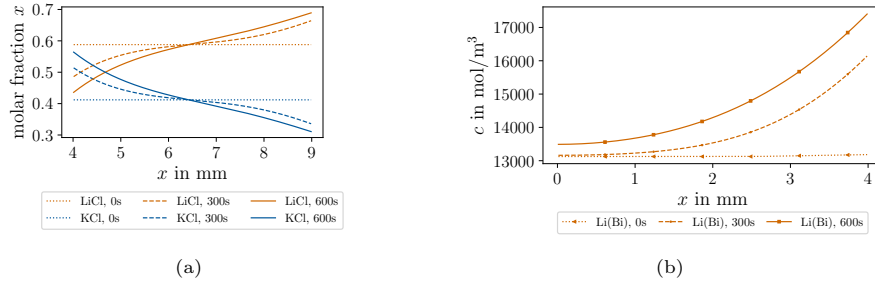


Figure 8: Species distribution for discharge current density $j_1 = -100\text{mA}/\text{cm}^2$ in (a) the Li|LiCl-KCl|Bi electrolyte and (b) Li(Bi) cathode for different discharge times.

open cell voltage of 0.9-1V was observed under comparable conditions [102, 103]. The reason for this deviation is simply that the activity coefficient was assumed to be one, when the activity of lithium in bismuth $a_{\text{Li}(\text{Bi})}$ is calculated. To “compensate” for this simplification, and to make the results more illustrative, the cell voltage is linearly shifted by +1V by adding a second axis to the figures.

As discussed in section 2.1, concentration and ohmic overpotential lower the cell voltage. Here it is important to mention that the OCV is updated in each time step based on the interface Li-concentration in the cathode. Therefore, the OCV curve already includes the concentration overpotential in the cathode. The orange curves in Fig. 9a show the cell voltage including concentration overpotentials in the electrolyte. It can be clearly seen that the latter have a significant influence on the cell voltage. Thus, it is not advisable to neglect them. In their recent study, Weber et al. [3] modelled the cell voltage of a Li||Bi cell without considering the concentration overpotentials in the electrolyte. Here, deviations between model and experiment were observed especially at high current densities (see e.g. Fig. 15a in [3]), which might be attributed in part to concentration effects in the electrolyte.

Lastly, the grey curves in Fig. 9a consider ohmic losses as well. In the simplest assumption, the entire current contributes to the ohmic loss in the cell. The present study shows that this is not the case since the measured terminal voltage (dotted blue line with triangle icon) does not match with the theoretical E (following Eq. (2), solid grey line with square icon). In contrast, when considering only the migrational current when calculating ohmic losses, the theoretical formula matches well with the simulation results. As it was already discussed previously, the diffusive current contributes to charge transfer and therefore increases – at least in the present case – the cell voltage and enhances the performance of the entire cell. Consequently, it can be stated that only the migrational part is important to define the ohmic loss.

In Fig. 9b, the overvoltages are explicitly shown, where $I_d R$ represents the

amount of lossless charge transfer expressed as “voltage gain⁵” for better clarification of its sign. It can be immediately seen that the ohmic overvoltage has the largest influence on the cell voltage. However, concentration overpotentials in the electrolyte are increasing with time and reach a similar value as the former. While the concentration overpotential at the anode-electrolyte interface is comparatively small and will approach steady state, it is larger and might approach infinity at the electrolyte-cathode interface.

Vallet et al. [47] found experimentally that the magnitude of concentration overpotentials in an $\text{AgNO}_3\text{-NaNO}_3$ electrolyte at 300°C and 150 mA/cm^2 varies between 5 to 15mV at each interface. Further, Braunstein et al. [44] predicted analytically that the concentration overpotential for a LiCl-KCl electrolyte at 450°C under ideal conditions would be about 17mV. Since the magnitude of the concentration overpotential in the present study (see Fig. 9b) is in the same range, it is emphasised that the concentration overpotentials in the electrolyte are indeed important and cannot be neglected.

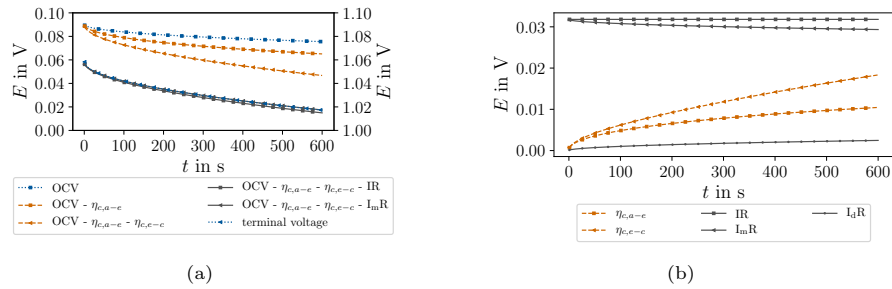


Figure 9: Analysis of (a) the cell voltage and (b) magnitude of overvoltages for discharge current density $j_1 = -100\text{mA/cm}^2$. The second axis in (a) describes a potential shift of +1V for better comparability with experimental results. Note that in (b) only absolute values are shown; the term $I_d R$ has in reality a negative sign.

Concentration typically depends on the square root of time in processes controlled by diffusion [104]. In Fig. 10 it can be seen that plotting $a_{\text{Li(Bi)}}$ versus the square root of time results in a nearly perfect straight line, a good indication that the transport in the cathode is – as expected – purely diffusive. In return, the transport in the electrolyte is not purely diffusive, since the linear fit of $a_{\text{Li}^+, \text{a-e}}$ does not entirely cover the simulated points. This indicates that migration in the boundary layer has to be taken into account. If fluid flow would be considered, convection would be important as well.

Besides analysing individual overvoltages and the corresponding phenomena, it is important to compare the impact of different current densities. Figure 11a shows, what is trivial: the terminal voltage decreases when the current

⁵Undoubtedly, there is no real voltage gain in the cell. This expression is used only as descriptive representation here.

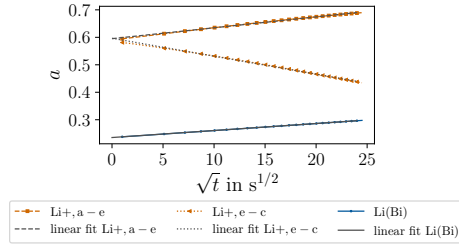


Figure 10: Parameter fit of activities for discharge current density $j_1 = -100\text{mA}/\text{cm}^2$.

density increases. Simultaneously the voltage losses increase. Regarding those, in Fig. 11b it can be observed that the ohmic losses dominate for short time or high currents where the concentration of the active ion in the electrolyte is far away from steady state. Especially, when the concentration in the electrolyte approaches zero at the cathode interface, the influence of the concentration overpotential increases exponentially. The corresponding effects at the anode and cathode interface are closely linked with activity, thus with concentration and concentration gradient of the species. In general that means: the higher the current density, the higher the concentration gradient; thus, the activity of lithium at the cathode approaches zero faster, while it approaches steady state faster at the anode interface. In galvanostatic operation, the former might lead to chronopotentiometric transition, i.e. a sudden cell voltage rise, and undesired electrochemical reactions [43].

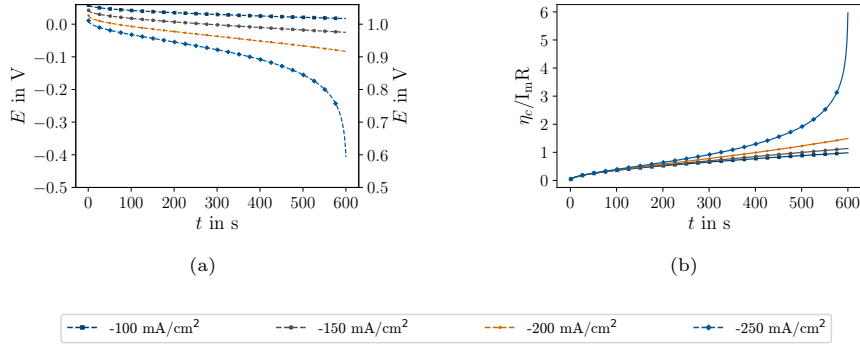


Figure 11: Comparison of (a) the cell voltage and (b) ratio of concentration overpotential to ohmic overpotential caused by migrational current for different discharge current densities. The second axis in (a) describes a potential shift of +1V for better comparability with experimental results.

Just as the overpotentials, the behaviour of the potential jumps at anode and cathode interface is similar. At the anode steady state is approached as

no solidification or other solubility threshold in the electrolyte is considered. In contrast, overpotential and jump at the cathode tend towards infinity due to the depletion of active ions.

Polarisation curves are used, amongst others, for fuel cells [105] to analyse the available electric power. Such a polarisation curve for the Li||Bi LMB is generated and shown in Fig. 12. In order to achieve realistic potentials, a constant activity coefficient of Li in Bi of $4.2 \cdot 10^{-5}$ m²/s is assumed [106]. Simulations are performed until reaching a steady state and with a sufficiently thick cathode to avoid any influence of (a lower) state of charge.

At first glance, the diagram shows precisely that there is a limiting current density, of approximately $j = -165\text{mA}/\text{cm}^2$, which is a little higher than the previously calculated $-130\text{mA}/\text{cm}^2$. Since not only diffusion – as considered in calculating the limiting current density – contributes to mass transfer in the boundary layer, migrational species transport can lead to an in- or decrease in the limiting current [107]. In case of the reactant ion – lithium in the present case – having a diffusive current density being considerably different from the other ions, the influence of migration on the limiting current density is expected to be quite high [75]. The ratio $j_{\text{lim}}/j_{\text{lim,d}} = 165/130 \approx 1.27$ indicates that migration enhances the limiting current by 27%. Conversely, this also means that the thickness of the boundary that determines the limiting current is reduced due to migrational species transport.

Overall, the three relevant types of overpotentials – as introduced in section 2.1 – can be identified. Of particular interest is the fact that the diffusive losses in the electrolyte increase largely with an increasing current. This indicates that the diffusive current density must also increase hereby. As the influence of the diffusive current density was discussed previously, this may lead to the assumption that the cell performance at higher current densities is more influenced by diffusion than at lower current. Appendix B further elaborates on the ratio of the different current density components. Moreover, the area beneath the polarisation curve shows the available electric power of the cell.

After the point where $\eta_c \approx \eta_\Omega$, which is at approximately $30\text{mA}/\text{cm}^2$, diffusive losses start to dominate the overpotentials in the cell. Here, it must be noted that this is a very small value compared to typical battery current densities, which are in the order of $200\text{--}300\text{mA}/\text{cm}^2$ [108]. Further, parallels to Fig. 11b can be seen: concentration overpotentials can – under certain conditions – exceed the ohmic losses.

Summing up, it has been shown that concentration overpotentials can have an important influence on the cell performance: the corresponding losses easily reach more than 50% of the total losses of electric power. This statement must, of course, be seen in context of the limitations of the model. The simplifications concerning the ion activity, which were introduced by Temkin’s model, seem to be justified. Molten salt experiments by Vallet gave similar concentration overpotentials. On the other hand, the obtained limiting current of $165\text{mA}/\text{cm}^2$ seems to be extremely small. In various Li||Bi cell experiments, ten times larger current densities were observed [73, 77, 108–110]. It is therefore obvious that convection must always be present in the electrolyte of real batteries and may be

triggered by a number of effects, likely in combination of several causes. While it is impossible to identify them with certainty, some can be ruled out. The Taylor instability cannot appear in small cells and thin layers [22, 24] and the metal pad roll instability would need much larger Li||Bi cells [14] to arise. While the critical Rayleigh numbers of internally heated convection [6, 9, 10, 55] are not exceeded for the 5 mm thin electrolyte and the moderate current densities in the paper at hand, internally heated convection is likely to occur for the higher current densities and thicker electrolyte layers used in experiments. Depending on the experimental setup, electro-vortex flows [8, 19], localised heating/cooling [8], solutal convection in the electrolyte, convection driven by viscous coupling from the cathode or anode [55], and Marangoni convection [9] are additional possible means to intensify mass transfer.

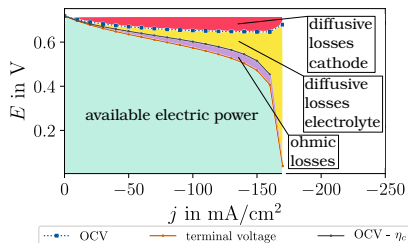


Figure 12: Polarisation curve of the Li|LiCl-KCl|Bi liquid metal battery.

6. Conclusion and Outlook

Concentration gradients and overpotentials in molten salt electrolytes have been well-known for more than forty years. However, when modelling liquid metal batteries, the latter have always been ignored – with the notable exception of the work of Newhouse [2]. With this motivation, mass transport in a Li||Bi concentration cell with a LiCl-KCl electrolyte is studied.

For this purpose, an OpenFOAM model relying on the parent-child mesh approach that is suitable for electrochemical simulations of LMBs is developed. The solver is able to calculate potential and species distribution in a full LMB where all three regions – anode, electrolyte and cathode – can be coupled. Further, modelling interfacial processes without resolving the electrical double layer microscopically or using experimental values is successfully realised using potential jumps and cyclic boundary conditions at both internal interfaces. The solver is thoroughly verified using four exemplary test cases and validated through a comparative study with experimental results.

Modelling a realistic Li||Bi LMB with a mixed cation electrolyte leads to three main conclusions. Firstly, it is confirmed that concentration gradients in the electrolyte are indeed important. Without convection, mass transfer overpotentials can reach or even exceed the ohmic losses. While the latter

appear instantaneous, concentration gradients develop rather slowly on a scale of several minutes. Reducing the cell potential by several tens of millivolts and leading to solidification of the electrolyte in the worst case, concentration gradients can by no means be ignored.

A second important finding concerns diffusive mass transport in the electrolyte. Depending on the relation of the diffusion coefficients between the electrolyte's species, the overall diffusive current can be directed in the same, or the opposite direction of the migrational current. Thus, it can "artificially" increase or reduce the ohmic overpotential. This means at the same time that computing the ohmic cell losses by the full cell current – instead of only the migrational current – will always be an estimate.

Finally, it is shown that the limiting current is difficult to predict for real cells. The diffusive limiting current density can simply be calculated, but underestimates the "true" value by 30% in our case as it does not account for migration. The fact that short circuit current densities were obtained in Li||Bi cell experiments, which exceed the simulated value by a factor of ten, is a clear evidence that convection must be present in the molten salt. The source and intensity of this flow shall therefore be subject of further investigation.

With this motivation, it appears recommendable to implement the Navier-Stokes equations into the present model and perform battery simulations with fluid motion. The fact that electrochemical transport is now successfully integrated in a finite volume solver is highly beneficial and a particularly good starting point for developing a solver that accounts for fluid flow as well. Likewise it could be important to consider phase change of the electrolyte dependent on the composition. Apart from enhancing the capabilities of the numerical solver, accurate values for diffusion coefficients as well as activities are fundamental to obtain reliable numerical results. Finally, the presented model can – with small changes – be applied to many other electrochemical devices. It is particularly well suited for modelling cells with sharp interfaces between electrode and electrolyte as well as with very thin double layers.

Acknowledgements

This project has received funding from the European Union's Horizon 2020 research and innovation program under grant agreement No. 963599 and in frame of the Helmholtz - RSF Joint Research Group "Magnetohydrodynamic instabilities: Crucial relevance for large scale liquid metal batteries and the sun-climate connection", contract No. HRSF-0044 and RSF-18-41-06201. We would like to thank K. E. Einarsrud, G. Mutschke, M. Huang, S. Beale and G. Natarajan for fruitful discussions about the electrochemical simulations.

Data availability statement

The solver and validation test case of Vallet et al. are openly available at <https://doi.org/10.14278/rodare.2313>.

Appendix A. Species transport equation

Solving the Poisson equation Eq. (19) gives results for the desired variables. But, using those values can lead to inaccurate results for the species transport. To avoid this, the potential gradient in Eq. (43) must be replaced. In the following it is shown, why φ or $\nabla\varphi$ cannot be taken directly, but require special care, when solving the species transport equation. To start, the most simple test case of an electrolyte with two ions and corresponding equal diffusion coefficients $D_- = D_+ = D$ and $\nu_- = -\nu_+$ is considered. Due to electroneutrality $c_- = c_+ = c$ follows. With this, Eq. (18) reduces to Eq. (6) and $\nabla\varphi = -\mathbf{j}/\sigma$. Having a closer look at the migration term $\nabla \cdot (\Psi c_i)$ in Eq. (42), the following can be found:

$$\nabla \cdot (\Psi c) = \nabla \cdot \left(\pm \nu_+ \frac{DF}{RT} \frac{\mathbf{j}}{\sigma} c \right). \quad (\text{A.1})$$

By simplifying Eq. (17) to $\sigma_{\text{salt}} = 2 \cdot F^2 D c \nu_+^2 / (RT)$ this leads to

$$\nabla \cdot \left(\pm \frac{\mathbf{j}}{2F\nu_+} \right) \Leftrightarrow \pm \frac{1}{2F\nu_+} (\nabla \cdot \mathbf{j}) \pm \mathbf{j} \cdot \nabla \left(\frac{1}{2F\nu_+} \right). \quad (\text{A.2})$$

Due to conservation of charge, the first term is zero. The second term is zero as well. So for the most simple case,

$$\nabla \cdot (\Psi c_i) = 0 \quad (\text{A.3})$$

must be satisfied. Now a closer look to a single cell is necessary. To meet the divergence-free condition, $c_i \nabla\varphi$ needs to be equal in the cell centre c and at the cell boundary b . Simply, this means that $c_b \frac{\partial\varphi}{\partial x} \Big|_b = c_c \frac{\partial\varphi}{\partial x} \Big|_c$ must be true, otherwise numerically generated divergence will occur. Due to the given boundary conditions, $c_b \neq c_c$ is valid. Therefore $\frac{\partial\varphi}{\partial x} \Big|_b \neq \frac{\partial\varphi}{\partial x} \Big|_c$ needs to be satisfied, too. Within OpenFOAM, gradient fields are computed using the Gauss integral, which means that the face values of the potential are integrated to obtain the cell-centred potential gradient [72]. However, this means also that the gradient of the potential is never computed on the boundary, but simply assumed to be the same as in the cell centre. Using such a gradient field directly would therefore lead to considerable calculation errors on the boundary itself.

Appendix B. Current density composition

Within the electrolyte, the current density consists – as shown in Eq. (18) – of a diffusive and migrational part. In order to examine the particular composition of the applied current density, some specific points below the detected limiting current are considered. The results are shown in Fig. B.13.

First, it is noticeable that the absolute value of the migrational current in the electrolyte is lower compared to the electrodes. This difference is compensated by the diffusional current so that charge conservation is ensured. With increasing cell current, the diffusional part increases concurrently. Since this has direct

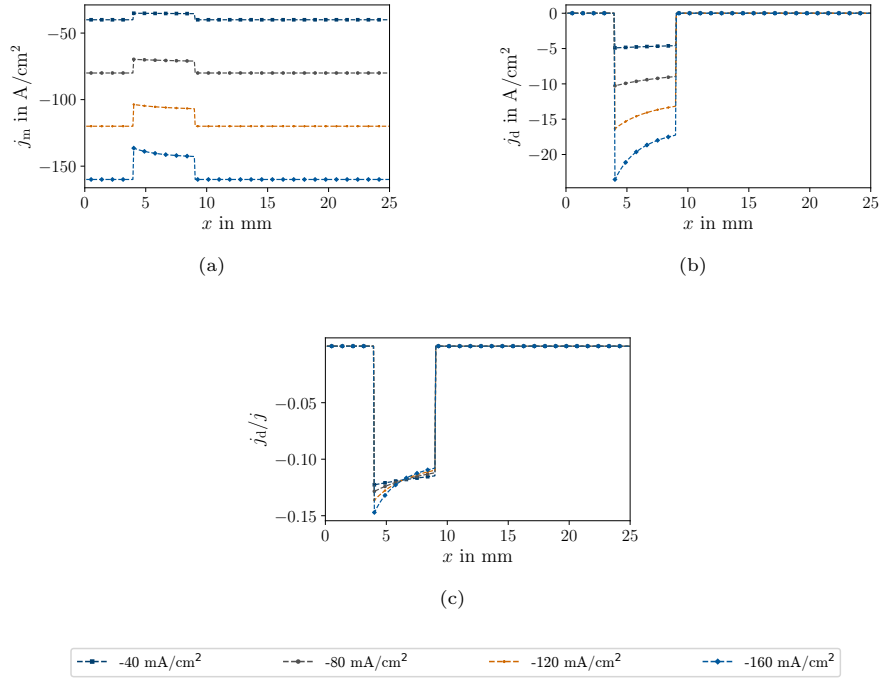


Figure B.13: Distribution of (a) migrational and (b) diffusive current density as well as (c) the ratio j_d/j over the cell domain at steady state species distribution for different discharge current densities.

influences on the charge transport in the electrolyte, it can be deduced that more lossless charge transfer is present that could enhance the cell performance of the battery. Nevertheless, the ratio j_d/j does not vary significantly for the investigated currents, which means that the general influence of the diffusive current is almost independent of the applied current.

References

- [1] H. Kim, D. A. Boysen, J. M. Newhouse, B. L. Spatocco, B. Chung, P. J. Burke, D. J. Bradwell, K. Jiang, A. A. Tomaszowska, K. Wang, W. Wei, L. A. Ortiz, S. A. Barriga, S. M. Poizeau, D. R. Sadoway, Liquid Metal Batteries: Past, Present, and Future, *Chemical Reviews* 113 (3) (2013) 2075–2099. doi:10.1021/cr300205k.
- [2] J. M. Newhouse, Modeling the Operating Voltage of Liquid Metal Battery Cells, Ph.D. thesis, Massachusetts Institute of Technology (2014).
- [3] N. Weber, C. Ducek, G. M. Horstmann, S. Landgraf, M. Nimtz, P. Personnettaz, T. Weier, D. R. Sadoway, Cell voltage model for Li-Bi liquid metal batteries, *Applied Energy* 309 (2022) 118331. doi:10.1016/j.apenergy.2021.118331.
- [4] D. Agarwal, R. Potnuru, C. Kaushik, V. R. Darla, K. Kulkarni, A. Garg, R. K. Gupta, N. Tiwari, K. S. Nalwa, Recent advances in the modeling of fundamental processes in liquid metal batteries, *Renewable and Sustainable Energy Reviews* 158 (2022) 112167. doi:10.1016/j.rser.2022.112167.
- [5] D. H. Kelley, T. Weier, Fluid Mechanics of Liquid Metal Batteries, *Applied Mechanics Reviews* 70 (2) (2018) 020801. doi:10.1115/1.4038699.
- [6] Y. Shen, O. Zikanov, Thermal convection in a liquid metal battery, *Theoretical and Computational Fluid Dynamics* 30 (4) (2016) 275–294. doi:10.1007/s00162-015-0378-1.
- [7] A. Beltrán, MHD natural convection flow in a liquid metal electrode, *Applied Thermal Engineering* 114 (2016) 1203–1212. doi:10.1016/j.applthermaleng.2016.09.006.
- [8] R. F. Ashour, D. H. Kelley, A. Salas, M. Starace, N. Weber, T. Weier, Competing forces in liquid metal electrodes and batteries, *Journal of Power Sources* 378 (2018) 301–310. doi:10.1016/j.jpowsour.2017.12.042.
- [9] T. Köllner, T. Boeck, J. Schumacher, Thermal Rayleigh-Marangoni convection in a three-layer liquid-metal-battery model, *Physical Review E* 95 (5) (2017) 053114. doi:10.1103/PhysRevE.95.053114.
- [10] P. Personnettaz, P. Beckstein, S. Landgraf, T. Köllner, M. Nimtz, N. Weber, T. Weier, Thermally driven convection in Li||Bi liquid metal batteries, *Journal of Power Sources* 401 (2018) 362–374. doi:10.1016/j.jpowsour.2018.08.069.
- [11] R. F. Ashour, Tackling key engineering challenges in liquid metal batteries: Temperature and mass transport, Ph.D. thesis, University of Rochester (2019).

- [12] D. F. Keogh, V. Timchenko, J. Reizes, C. Menictas, Modelling Rayleigh-Bénard convection coupled with electro-vortex flow in liquid metal batteries, *Journal of Power Sources* 501 (2021) 229988. doi:[10.1016/j.jpowsour.2021.229988](https://doi.org/10.1016/j.jpowsour.2021.229988).
- [13] O. Zikanov, Metal pad instabilities in liquid metal batteries, *Physical Review E* 92 (6) (2015) 063021. doi:[10.1103/PhysRevE.92.063021](https://doi.org/10.1103/PhysRevE.92.063021).
- [14] N. Weber, P. Beckstein, W. Herreman, G. M. Horstmann, C. Nore, F. Stefani, T. Weier, Sloshing instability and electrolyte layer rupture in liquid metal batteries, *Physics of Fluids* 29 (5) (2017) 054101. doi:[10.1063/1.4982900](https://doi.org/10.1063/1.4982900).
- [15] G. M. Horstmann, N. Weber, T. Weier, Coupling and stability of interfacial waves in liquid metal batteries, *Journal of Fluid Mechanics* 845 (2018) 1–35. doi:[10.1017/jfm.2018.223](https://doi.org/10.1017/jfm.2018.223).
- [16] S. Molokov, The nature of interfacial instabilities in liquid metal batteries in a vertical magnetic field, *Europhysics Letters* 121 (4) (2018) 44001. doi:[10.1209/0295-5075/121/44001](https://doi.org/10.1209/0295-5075/121/44001).
- [17] A. Tucs, V. Bojarevics, K. Pericleous, MHD stability of large scale liquid metal batteries, *Journal of Fluid Mechanics* 852 (2018) 453–483.
- [18] O. Zikanov, Shallow water modeling of rolling pad instability in liquid metal batteries, *Theoretical and Computational Fluid Dynamics* 32 (3) (2018) 325–347.
- [19] W. Herreman, C. Nore, P. Ziebell Ramos, L. Cappanera, J.-L. Guermond, N. Weber, Numerical simulation of electrovortex flows in cylindrical fluid layers and liquid metal batteries, *Physical Review Fluids* 4 (11) (2019) 113702. doi:[10.1103/PhysRevFluids.4.113702](https://doi.org/10.1103/PhysRevFluids.4.113702).
- [20] F. Stefani, T. Weier, T. Gundrum, G. Gerbeth, How to circumvent the size limitation of liquid metal batteries due to the Tayler instability, *Energy Conversion and Management* 52 (2011) 2982–2986. doi:[10.1016/j.enconman.2011.03.003](https://doi.org/10.1016/j.enconman.2011.03.003).
- [21] N. Weber, V. Galindo, F. Stefani, T. Weier, T. Wondrak, Numerical simulation of the Tayler instability in liquid metals, *New Journal of Physics* 15 (4) (2013) 043034. doi:[10.1088/1367-2630/15/4/043034](https://doi.org/10.1088/1367-2630/15/4/043034).
- [22] N. Weber, V. Galindo, F. Stefani, T. Weier, Current-driven flow instabilities in large-scale liquid metal batteries, and how to tame them, *Journal of Power Sources* 265 (2014) 166–173. doi:[10.1016/j.jpowsour.2014.03.055](https://doi.org/10.1016/j.jpowsour.2014.03.055).
- [23] N. Weber, V. Galindo, J. Priede, F. Stefani, T. Weier, The influence of current collectors on Tayler instability and electro-vortex flows in liquid metal batteries, *Physics of Fluids* 27 (1) (2015) 014103. doi:[10.1063/1.4905325](https://doi.org/10.1063/1.4905325).

- [24] W. Herreman, C. Nore, L. Capanera, J.-L. Guermond, Tayler instability in liquid metal columns and liquid metal batteries, *Journal of Fluid Mechanics* 771 (2015) 79–114. doi:[10.1017/jfm.2015.159](https://doi.org/10.1017/jfm.2015.159).
- [25] N. Weber, P. Beckstein, V. Galindo, M. Starace, T. Weier, Electro-vortex flow simulation using coupled meshes, *Computers & Fluids* 168 (2018) 101–109. doi:[10.1016/j.compfluid.2018.03.047](https://doi.org/10.1016/j.compfluid.2018.03.047).
- [26] N. Weber, M. Nimtz, P. Personnetaz, A. Salas, T. Weier, Electromagnetically driven convection suitable for mass transfer enhancement in liquid metal batteries, *Applied Thermal Engineering* 143 (2018) 293–301. doi:[10.1016/j.applthermaleng.2018.07.067](https://doi.org/10.1016/j.applthermaleng.2018.07.067).
- [27] B. Agruss, H. R. Karas, V. L. Decker, Design and development of a liquid metal fuel cell, Tech. Rep. ASD-TDR-62-1045, General Motors Corporation (1962).
- [28] J. M. Newhouse, D. R. Sadoway, Charge-Transfer Kinetics of Alloying in Mg-Sb and Li-Bi Liquid Metal Electrodes, *Journal of The Electrochemical Society* 164 (12) (2017) A2665–A2669. doi:[10.1149/2.1571712jes](https://doi.org/10.1149/2.1571712jes).
- [29] H. Shimotake, E. J. Cairns, Bimetallic galvanic cells with fused-salt electrolytes, in: *Advances in Energy Conversion Engineering*, American Society of Mechanical Engineers New York, 1967, pp. 951–962.
- [30] R. C. Vogel, E. R. Proud, J. Royal, Chemical engineering division research highlights, Tech. Rep. ANL-7450, Argonne National Laboratory (1968).
- [31] R. C. Vogel, M. Levenson, E. R. Proud, J. Royal, Chemical engineering division annual report - 1968, Tech. Rep. ANL-7575, Argonne National Laboratory (1969).
- [32] B. Agruss, H. R. Karas, The Thermally Regenerative Liquid Metal Concentration Cell, in: C. E. Crouthamel, H. L. Recht (Eds.), *Regenerative EMF Cells*, Vol. 64 of *Advances in Chemistry*, American Chemical Society, Washington, D.C., 1967, pp. 62–81.
- [33] L. A. Herédy, M. L. Iverson, G. D. Ulrich, H. L. Recht, Development of a thermally regenerative Sodium-Mercury galvanic system Part I Electrochemical and Chemical Behavior of Sodium-Mercury Galvanic Cells, in: C. E. Crouthamel, H. L. Recht (Eds.), *Regenerative EMF Cells*, American Chemical Society, 1967, pp. 30–42.
- [34] M. S. Foster, Laboratory Studies of Intermetallic Cells, in: C. E. Crouthamel, H. L. Recht (Eds.), *Regenerative EMF Cells*, American Chemical Society, 1967, pp. 136–148.
- [35] B. Agruss, The Thermally Regenerative Liquid-Metal Cell, *Journal of The Electrochemical Society* 110 (11) (1963) 1097–1103.

- [36] R. C. Vogel, M. Levenson, F. R. Masten, Chemical engineering division semiannual report, Tech. Rep. ANL-6925, Argonne National Laboratory (1965).
- [37] R. C. Vogel, M. Levenson, E. R. Proud, J. Royal, Chemical engineering division research highlights, Tech. Rep. ANL-7350, Argonne National Laboratory (1967).
- [38] A. Blanchard, Enabling multi-cation electrolyte usage in LMBs for lower cost and operating temperature (2013).
- [39] T. Ouchi, H. Kim, B. L. Spatocco, D. R. Sadoway, Calcium-based multi-element chemistry for grid-scale electrochemical energy storage, *Nature Communications* 7 (2016) 10999. doi:10.1038/ncomms10999.
- [40] S. J. Percival, L. J. Small, E. D. Spoecker, Electrochemistry of the NaI-AlCl₃ Molten Salt System for Use as Catholyte in Sodium Metal Batteries, *Journal of The Electrochemical Society* 165 (14) (2018) A3531–A3536. doi:10.1149/2.1191814jes.
- [41] Q. Gong, W. Ding, A. Bonk, H. Li, K. Wang, A. Jianu, A. Weisenburger, A. Bund, T. Bauer, Molten iodide salt electrolyte for low-temperature low-cost sodium-based liquid metal battery, *Journal of Power Sources* 475 (2020) 228674. doi:10.1016/j.jpowsour.2020.228674.
- [42] M. M. Gross, S. J. Percival, L. J. Small, J. Lamb, A. S. Peretti, E. D. Spoecker, Low-Temperature Molten Sodium Batteries, *ACS Applied Energy Materials* 3 (11) (2020) 11456–11462. doi:10.1021/acsaem.0c02385.
- [43] C. E. Vallet, J. Braunstein, Steady-State Composition Profiles in Mixed Molten Salt Electrochemical Devices: I. Lithium/Sulfur Battery Analogs, *Journal of The Electrochemical Society* 125 (8) (1978) 1193–1198. doi:10.1149/1.2131648.
- [44] J. Braunstein, C. E. Vallet, Migrational Polarization in High Current Density Molten Salt Battery and Fuel Cell Analogs, *Journal of The Electrochemical Society* 126 (6) (1979) 960–965. doi:10.1149/1.2129202.
- [45] C. E. Vallet, D. E. Heatherly, J. Braunstein, Composition Gradients in Molten Salt Binary Mixtures during Electrolysis at High Current Density, *Journal of The Electrochemical Society* 127 (1) (1980) 1–7. doi:10.1149/1.2129617.
- [46] C. E. Vallet, L. M. Kidd, D. E. Heatherly, R. L. Sherman, J. Braunstein, SEM/EDX and AA Measurements of Current-Induced Composition Gradients. Molten NaNO₃-AgNO₃ in Porous Yttria, *Journal of The Electrochemical Society* 129 (5) (1982) 931–935. doi:10.1149/1.2124068.

- [47] C. E. Vallet, D. E. Heatherly, R. L. Sherman, J. Braunstein, Current-Induced Composition Gradients in Molten $\text{AgNO}_3\text{-NaNO}_3$: A Model System for the LiCl-KCl Electrolyte of an Li/S Battery, *Journal of The Electrochemical Society* 129 (1) (1982) 49–55. doi:10.1149/1.2123790.
- [48] C. E. Vallet, D. E. Heatherly, J. Braunstein, Composition Gradients in Electrolyzed LiCl-KCl Eutectic Melts, *Journal of The Electrochemical Society* 130 (12) (1983) 2366–2370. doi:10.1149/1.2119588.
- [49] P. Masset, R. A. Guidotti, Thermal activated (thermal) battery technology: Part ii. molten salt electrolytes, *Journal of Power Sources* 164 (1) (2007) 397–414. doi:10.1016/j.jpowsour.2006.10.080.
- [50] N. Weber, S. Landgraf, K. Mushtaq, M. Nimtz, P. Personnettaz, T. Weier, J. Zhao, D. Sadoway, Modeling discontinuous potential distributions using the finite volume method, and application to liquid metal batteries, *Electrochimica Acta* 318 (2019) 857–864. doi:10.1016/j.electacta.2019.06.085.
- [51] D. H. Kelley, D. R. Sadoway, Mixing in a liquid metal electrode, *Physics of Fluids* 26 (5) (2014) 057102. doi:10.1063/1.4875815.
- [52] P. Personnettaz, S. Landgraf, M. Nimtz, N. Weber, T. Weier, Mass transport induced asymmetry in charge/discharge behavior of liquid metal batteries, *Electrochemistry Communications* 105 (2019) 106496. doi:10.1016/j.elecom.2019.106496.
- [53] P. Personnettaz, S. Landgraf, M. Nimtz, N. Weber, T. Weier, Effects of current distribution on mass transport in the positive electrode of a liquid metal battery, *Magnetohydrodynamics* 56 (2-3) (2020) 247–254. doi:10.22364/mhd.56.2-3.16.
- [54] W. Herreman, S. Bénard, C. Nore, P. Personnettaz, L. Cappanera, J.-L. Guermond, Solutal buoyancy and electrovortex flow in liquid metal batteries, *Physical Review Fluids* 5 (7) (2020) 074501. doi:10.1103/PhysRevFluids.5.074501.
- [55] P. Personnettaz, T. S. Klopper, N. Weber, T. Weier, Layer coupling between solutal and thermal convection in liquid metal batteries, *International Journal of Heat and Mass Transfer* 188 (2022) 122555. doi:10.1016/j.ijheatmasstransfer.2022.122555.
- [56] N. Weber, M. Nimtz, P. Personnettaz, T. Weier, D. Sadoway, Numerical simulation of mass transfer enhancement in liquid metal batteries by means of electro-vortex flow, *Journal of Power Sources Advances* 1 (2020) 100004. doi:10.1016/j.powera.2020.100004.
- [57] W. Herreman, C. Nore, L. Cappanera, J.-L. Guermond, Efficient mixing by swirling electrovortex flows in liquid metal batteries, *Journal of Fluid Mechanics* 915 (2021) A17. doi:10.1017/jfm.2021.79.

- [58] W. Herreman, S. Bénard, C. Nore, P. Personnetaz, L. Cappanera, J.-L. Guermond, Solutal buoyancy and electrovortex flow in liquid metal batteries, *Physical Review Fluids* 5 (7) (2020) 074501. [doi:10.1103/PhysRevFluids.5.074501](https://doi.org/10.1103/PhysRevFluids.5.074501).
- [59] R. F. Ashour, D. H. Kelley, Convection-Diffusion Model of Lithium-Bismuth Liquid Metal Batteries, in: G. Lambotte, J. Lee, A. Allanore, S. Wagstaff (Eds.), *Materials Processing Fundamentals 2018*, Springer International Publishing, Cham, 2018, pp. 41–52. [doi:10.1007/978-3-319-72131-6_4](https://doi.org/10.1007/978-3-319-72131-6_4).
- [60] T. L. Aguilar-García, M. Rivero, J. Núñez, I. Alfonso, A. Beltrán, Effect of electromagnetically driven liquid metal flows on the electric potential difference in a cuboid vessel, *Journal of Power Sources* 483 (2021) 229162. [doi:10.1016/j.jpowsour.2020.229162](https://doi.org/10.1016/j.jpowsour.2020.229162).
- [61] N. Weber, V. Galindo, F. Stefani, T. Weier, The Tayler instability at low magnetic Prandtl numbers: Between chiral symmetry breaking and helicity oscillations, *New Journal of Physics* 17 (11) (2015) 113013. [doi:10.1088/1367-2630/17/11/113013](https://doi.org/10.1088/1367-2630/17/11/113013).
- [62] C. Hirsch, *Numerical Computation of Internal and External Flows: Fundamentals of Computational Fluid Dynamics*, 2nd Edition, Elsevier/Butterworth-Heinemann, Oxford; Burlington, MA, 2007.
- [63] S. R. Idelsohn, E. Oñate, Finite volumes and finite elements: Two ‘good friends’, *International Journal for Numerical Methods in Engineering* 37 (19) (1994) 3323–3341. [doi:10.1002/nme.1620371908](https://doi.org/10.1002/nme.1620371908).
- [64] E. Fontes, FEM vs. FVM, <https://www.comsol.com/blogs/fem-vs-fvm/> (2018).
- [65] S. B. Beale, H. K. Roth, A. Le, D. H. Jeon, Development of an open source software library for solid oxide fuel cells, Tech. Rep. NRCC 53179, National Research Council Canada (2013).
- [66] S. B. Beale, H.-W. Choi, J. G. Pharoah, H. K. Roth, H. Jasak, D. H. Jeon, Open-source computational model of a solid oxide fuel cell, *Computer Physics Communications* 200 (2016) 15–26. [doi:10.1016/j.cpc.2015.10.007](https://doi.org/10.1016/j.cpc.2015.10.007).
- [67] J. Lück, A. Latz, Theory of reactions at electrified interfaces, *Physical Chemistry Chemical Physics* 18 (27) (2016) 17799–17804. [doi:10.1039/C6CP02681H](https://doi.org/10.1039/C6CP02681H).
- [68] S. V. Patankar, C. H. Liu, E. M. Sparrow, Fully Developed Flow and Heat Transfer in Ducts Having Streamwise-Periodic Variations of Cross-Sectional Area, *Journal of Heat Transfer* 99 (2) (1977) 180–186. [doi:10.1115/1.3450666](https://doi.org/10.1115/1.3450666).

- [69] S. B. Beale, Laminar Fully Developed Flow and Heat Transfer in an Offset Rectangular Plate-fin Surface, *PHOENICS Journal of Computational Fluid Dynamics and its Applications* 3 (1) (1990) 1–19.
- [70] S. B. Beale, D. B. Spalding, Numerical study of fluid flow and heat transfer in tube banks with stream-wise periodic boundary conditions, *Transactions of the Canadian Society for Mechanical Engineering* 22 (4A) (1998) 397–416. doi:[10.1139/tcsme-1998-0022](https://doi.org/10.1139/tcsme-1998-0022).
- [71] A. S. Moreira Ribeiro, Implementation and Analysis of a Semi-Empirical Vortex Generator Model in OpenFOAM, Master's thesis, TU Delft, Delft (2017).
- [72] C. J. Greenshields, OpenFOAM programmer's guide, OpenFOAM Foundation Ltd (2015).
- [73] D. A. J. Swinkels, Molten Salt Batteries and Fuel Cells, in: J. Braunstein, G. Mamantov, G. P. Smith (Eds.), *Advances in Molten Salt Chemistry*, Springer US, Boston, MA, 1971, pp. 165–223. doi:[10.1007/978-1-4757-0504-1_4](https://doi.org/10.1007/978-1-4757-0504-1_4).
- [74] K. J. Vetter, *Electrochemical Kinetics*, Academic Press, New York, 1967.
- [75] J. S. Newman, K. E. Thomas-Alyea, *Electrochemical Systems*, 3rd Edition, J. Wiley, Hoboken, N.J., 2004.
- [76] H. G. Weller, G. Tabor, H. Jasak, C. Fureby, A tensorial approach to computational continuum mechanics using object-oriented techniques, *Computers in Physics* 12 (6) (1998) 620–631. doi:[10.1063/1.168744](https://doi.org/10.1063/1.168744).
- [77] H. Shimotake, G. L. Rogers, E. J. Cairns, Secondary Cells with Lithium Anodes and Immobilized Fused-Salt Electrolytes, *Industrial & Engineering Chemistry Process Design and Development* 8 (1) (1969) 51–56. doi:[10.1021/i260029a009](https://doi.org/10.1021/i260029a009).
- [78] T. Takayama, M. Yoneda, Modeling of thermal and electric behavior of stacked Lithium-ion cells in OpenFOAM (2011).
- [79] J.-F. Wax, M. Johnson, L. Bove, M. Mihalkovic, Multi-Scale Study of the Static Structure of Liquid Li₇₀-Bi₃₀ Alloy, *EPJ Web of Conferences* 15 (2011) 01002. doi:[10.1051/epjconf/20111501002](https://doi.org/10.1051/epjconf/20111501002).
- [80] G. Steinleitner, W. Freyland, F. Hensel, Electrical conductivity and excess volume of the liquid alloy system Li-Bi, *Berichte der Bunsengesellschaft für physikalische Chemie* 79 (12) (1975) 1186–1189. doi:[10.1002/bbpc.19750791204](https://doi.org/10.1002/bbpc.19750791204).
- [81] B. Morgan, P. A. Madden, Ion mobilities and microscopic dynamics in liquid (Li,K)Cl, *The Journal of Chemical Physics* 120 (3) (2004) 1402–1413. doi:[10.1063/1.1629076](https://doi.org/10.1063/1.1629076).

- [82] J.-L. Burgot, *The Notion of Activity in Chemistry*, Springer International Publishing, Cham, 2017. doi:10.1007/978-3-319-46401-5.
- [83] M. Salanne, C. Simon, P. Turq, P. A. Madden, Calculation of Activities of Ions in Molten Salts with Potential Application to the Pyroprocessing of Nuclear Waste, *The Journal of Physical Chemistry B* 112 (4) (2008) 1177–1183. doi:10.1021/jp075299n.
- [84] M. Temkin, Mixtures of fused salts as ionic solutions, *Acta Physicochimica URSS* 20 (1945) 411–420.
- [85] P. Fellner, Comments on some models of molten salt mixtures, *Chemické Zvesti* 37 (5) (1983) 609–615.
- [86] P. Beckstein, V. Galindo, V. Vukčević, Efficient solution of 3D electromagnetic eddy-current problems within the finite volume framework of OpenFOAM, *Journal of Computational Physics* 344 (2017) 623–646. doi:10.1016/j.jcp.2017.05.005.
- [87] H. Jasak, Error analysis and estimation for the finite volume method with applications to fluid flows, Ph.D. thesis, Imperial College, London (1996).
- [88] S. Popinet, An accurate adaptive solver for surface-tension-driven interfacial flows, *Journal of Computational Physics* 228 (16) (2009) 5838–5866. doi:10.1016/j.jcp.2009.04.042.
- [89] R. Thirumalaisamy, G. Natarajan, A. Dalal, Towards an improved conservative approach for simulating electrohydrodynamic two-phase flows using volume-of-fluid, *Journal of Computational Physics* 367 (2018) 391–398. doi:10.1016/j.jcp.2018.04.024.
- [90] T. Iida, R. I. L. Guthrie, *The Physical Properties of Liquid Metals*, Clarendon Press, Oxford, 1988.
- [91] T. Iida, R. I. L. Guthrie, *The Thermophysical Properties of Metallic Liquids*, Oxford University Press, United Kingdom, 2015.
- [92] G. J. Janz, R. P. T. Tomkins, C. B. Allen, J. R. Downey, G. L. Garner, U. Krebs, S. K. Singer, Molten salts: Volume 4, part 2, chlorides and mixtures – electrical conductance, density, viscosity, and surface tension data, *Journal of Physical and Chemical Reference Data* 4 (4) (1975) 871–1178. doi:10.1063/1.555527.
- [93] C. Caccamo, M. Dixon, Molten alkali-halide mixtures: a molecular-dynamics study of Li/KCl mixtures, *Journal of Physics C: Solid State Physics* 13 (10) (1980) 1887–1900. doi:10.1088/0022-3719/13/10/009.
- [94] F. Lantelme, P. Turq, Ionic dynamics in the LiCl–KCl system at liquid state, *The Journal of Chemical Physics* 77 (6) (1982) 3177–3187. doi:10.1063/1.444192.

- [95] M. Hiroi, H. Shimotake, Effective conductivities of an FeS positive in LiCl-KCl eutectic electrolyte at different states of charge, *Journal of Applied Electrochemistry* 14 (1984) 341 – 347.
- [96] C.-C. Yang, Transport property of cations Li^+ and K^+ in the molten salt electrolyte, *Journal of the Chinese Institute of Engineers* 17 (6) (1994) 835–842. doi:10.1080/02533839.1994.9677652.
- [97] M. C. C. Ribeiro, Chemla Effect in Molten LiCl/KCl and LiF/KF Mixtures, *The Journal of Physical Chemistry B* 107 (18) (2003) 4392–4402. doi:10.1021/jp027261a.
- [98] Z. Chen, M. L. Zhang, W. Han, Z. Y. Hou, Y. De Yan, Electrodeposition of Li and electrochemical formation of Mg–Li alloys from the eutectic LiCl–KCl, *Journal of Alloys and Compounds* 464 (1-2) (2008) 174–178. doi:10.1016/j.jallcom.2007.10.019.
- [99] A. Bengtson, H. O. Nam, S. Saha, R. Sakidja, D. Morgan, First-principles molecular dynamics modeling of the LiCl–KCl molten salt system, *Computational Materials Science* 83 (2014) 362–370. doi:10.1016/j.commatsci.2013.10.043.
- [100] J. Wang, J. Wu, Z. Sun, G. Lu, J. Yu, Molecular dynamics study of the transport properties and local structures of molten binary systems (Li, Na)Cl, (Li, K)Cl and (Na, K)Cl, *Journal of Molecular Liquids* 209 (2015) 498–507. doi:10.1016/j.molliq.2015.06.021.
- [101] X. Zhou, C. Gao, Y. Shen, H. Li, S. Yan, H. Zhou, K. Wang, K. Jiang, Multi-field coupled model for liquid metal battery: Comparative analysis of various flow mechanisms and their effects on mass transfer and electrochemical performance, *Energy Reports* 8 (2022) 5510–5521. doi:10.1016/j.egy.2022.04.018.
- [102] H. L. Chum, R. A. Osteryoung, Review of Thermally Regenerative Electrochemical Cells, Solar Energy Research Institute, 1981.
- [103] E. J. Cairns, H. Shimotake, High-Temperature Batteries, *Science* 164 (3886) (1969) 1347–1355. doi:10.1126/science.164.3886.1347.
- [104] C. M. A. Brett, A. M. O. Brett, *Electrochemistry: Principles, Methods, and Applications*, Oxford University Press, 1993.
- [105] E. A. Heider, Der Einfluss der Adsorption auf die Sauerstoffreduktionsreaktion, Ph.D. thesis, Universität Ulm (2017).
- [106] Z. Cao, W. Xie, P. Chartrand, S. Wei, G. Du, Z. Qiao, Thermodynamic assessment of the Bi-alkali metal (Li, Na, K, Rb) systems using the modified quasichemical model for the liquid phase, *Calphad* 46 (2014) 159–167. doi:10.1016/j.calphad.2014.04.001.

- [107] V. S. Bagotskii, *Fundamentals of Electrochemistry*, 2nd Edition, The Electrochemical Society Series, Wiley-Interscience, Hoboken, N.J., 2006.
- [108] X. Ning, Satyajit Phadke, B. Chung, H. Yin, P. Burke, D. R. Sadoway, Self-healing Li–Bi liquid metal battery for grid-scale energy storage, *Journal of Power Sources* 275 (2015) 370–376. doi:10.1016/j.jpowsour.2014.10.173.
- [109] E. J. Cairns, R. K. Steunenbergh, High-temperature batteries, in: C. Rouse (Ed.), *Progress in High Temperature Physics and Chemistry*, Vol. 5, Pergamon Press, 1973, pp. 63–124.
- [110] N. V. Temnogorova, I. G. Volfson, A. I. Demidov, A. G. Morachevskii, Use of anodic chronopotentiometry for determining diffusion coefficients in molten alloys, *Elektrokhimiya* 16 (1979) 419–421.

Supplementary material S1. Comparison and verification with COM-SOL results

Supplementary material S1.1. Test case 1

Simulation results related to test case 1 are shown in Fig. S1.14. Due to $D_{\text{Cl}^-} = D_{\text{Li}^+}$, the species distribution and species concentration gradient for the Li^+ and Cl^- ions are equal, since the electroneutrality condition Eq. (15) is preserved within a tolerance of machine accuracy. Further, point symmetrical behaviour of the species distribution – as Eq. (23) and Eq. (24) as well as Fig. S1.14c show – is associated with equal concentration gradients. Pursuing Eq. (18) indicates that the corresponding electric conductivity following Eq. (18) needs to be symmetric as well. Furthermore, a symmetric trend in the electrolyte is also observable for the potential gradient in Fig. S1.14b, as the latter is linearly dependent on the species gradient (see Eq. (18)). Besides that, the diffusive current density of the Li^+ and Cl^- ions differs only in terms of a reversed sign. Hence, it can be concluded that the simulation satisfies the theory by confirming that the diffusive current density is zero.

In terms of verification, it can be seen that the solutions of OpenFOAM and COMSOL are in good agreement and match perfectly with each other in every case except of the species gradient at t_0 . Initial OpenFOAM results are analytically confirmed, whereas the initial COMSOL results are not reliable.

Supplementary material S1.2. Test case 2

As well as in test case 1, validity can be confirmed since the results of COMSOL and OpenFOAM shown in Fig. S1.15 match perfectly except for the diffusive current density in COMSOL at the initial time step.

Species distribution and gradient, diffusive current density and electric conductivity exhibit the same behaviour as outlined in the previous section. However, the potential gradient in the electrolyte is no longer symmetric. Here, it can be concluded that the diffusive current density has a significant influence on the potential gradient. Additionally and in contrast to test case 1, the potential changes over time. As the slope of the potential curve flattens in the electrolyte region over time, the electric conductivity there seems to increase. This may indicate that the electric loss in the electrolyte

$$U = \frac{\mathbf{j}l}{\sigma} \quad (\text{A.1})$$

with l being the resistor length, decreases over time. But, the electric conductivity is constant on average during the whole simulation. With this, it is made clear that the diffusive current density influences the electric losses significantly.

Supplementary material S1.3. Test case 3

Comparing OpenFOAM to COMSOL results for test case 3 – as presented in Fig. S1.16 and Fig. S1.17 shows validity of the former.

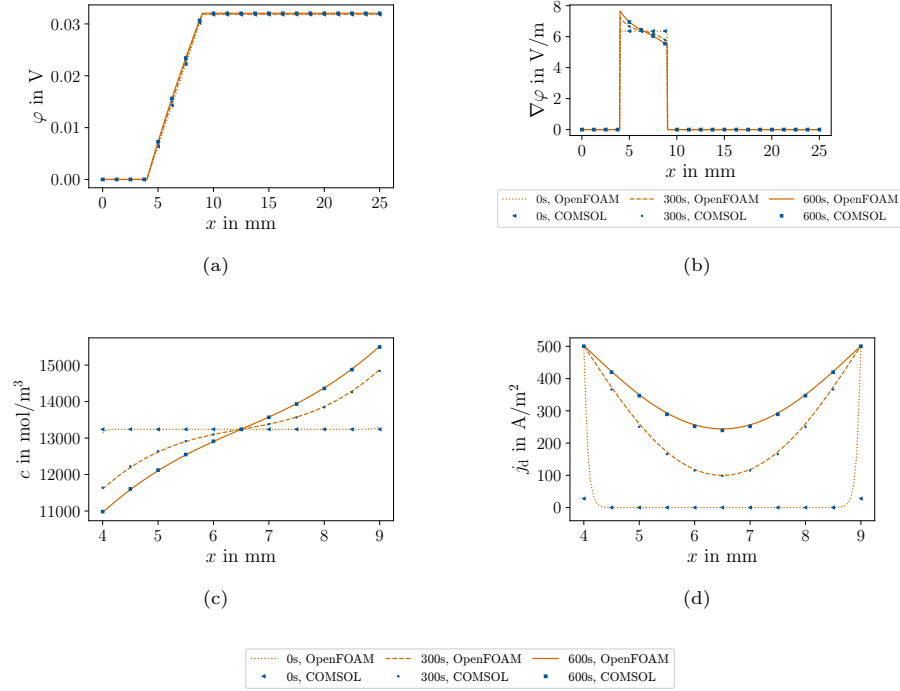


Figure S1.14: Test case 1; results for OpenFOAM and COMSOL simulations: (a) potential distribution (b) potential gradient in the whole cell, (c) species distribution and (d) diffusive current density of the Li^+ ion in the electrolyte.

In terms of the electric loss identifiable by the temporal development of the potential distribution, the conclusions drawn in the previous case can be confirmed as non-random. In contrast to the previous binary test cases, it can be seen in Fig. S1.17 that the species distributions and gradients – here expressed as diffusive current density – for a ternary electrolyte are not equal any more. Nevertheless, the electric conductivity σ is constant on average over time. For the Cl^- ion, being the common ion in both salts, the species distribution is symmetric, while this is not the case for the Li^+ and K^+ ions. This can be explained by the differing diffusion coefficients. Moreover, an asymmetric potential gradient is – as in test case 2 – observable within the electrolyte. This leads to the logical consequence that the reason for the asymmetry must lie in the diffusive part of the material balance for the species transport Eq. (20).

Supplementary material S1.4. Test case 4

In Fig. S1.18 the potential distribution in the cell, where the two potential jumps are clearly visible, is shown. Since $\nabla\varphi_{\text{case4}} \approx \nabla\varphi_{\text{case3}}$, the potential gradient is not presented again and it is referred to Fig. S1.16b. As in the

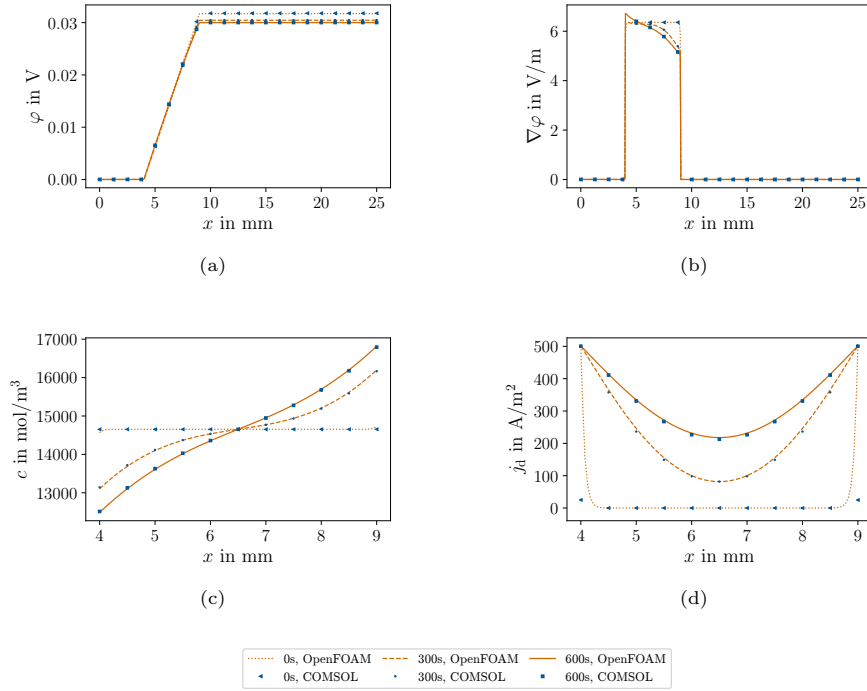


Figure S1.15: Test case 2; results for OpenFOAM and COMSOL simulations: (a) potential distribution (b) potential gradient in the whole cell, (c) species distribution and (d) diffusive current density of the Li^+ ion in the electrolyte.

previous verification test cases, the results of OpenFOAM and COMSOL match very well except for the initial time step.

Supplementary material S2. Grid study

A grid study for test case 3 is performed, to show that the results do not contain grid dependent errors. All simulations presented in section 4 and [Supplementary material S1](#) were done with a uniform grid spacing of $\Delta x_4 = 5 \cdot 10^{-5} \text{m}$. Here, $\Delta x_1 = 5 \cdot 10^{-4} \text{m}$, $\Delta x_2 = 2.5 \cdot 10^{-4} \text{m}$ and $\Delta x_3 = 1 \cdot 10^{-4} \text{m}$. The relative error between the larger grid spacing to the smaller grid spacing is calculated for potential, potential gradient, species distribution and species gradient of Li^+ and the results are shown in Fig. S2.19. It can be seen clearly that the error shows peaks at the interfaces between electrolyte and electrode which are decreasing, when the number of cells is increased. When the finest grid is used, the error is less than 1%, which is small enough to claim that the solutions, shown in section 4 and [Supplementary material S1](#) are grid independent.

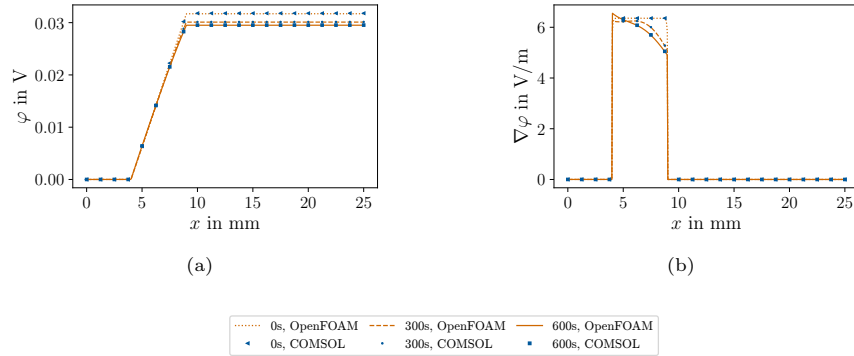


Figure S1.16: Test case 3; results for OpenFOAM and COMSOL simulations: (a) potential distribution (b) potential gradient in the whole cell.

Supplementary material S3. Electroneutrality study

As it was mentioned in section 2.3.2, the solver is able to differentiate, if a species is active or passive. The results should be the same no matter which species in the electrolyte is calculated from electroneutrality. So, it is investigated, if there are any differences in the solution of test case 3 when either Li^+ , Cl^- or K^+ are calculated from electroneutrality. The former is taken as reference case.

Fig. S3.20 shows that the error in the electric conductivity is less than 0.01%. Further, it can be seen in Fig. S3.21 that the species distribution and the species gradient in the electrolyte are almost the same for all three simulations. This means that the solver is robust and it is not necessary to add additional boundary conditions for the active species as it is needed in COMSOL.

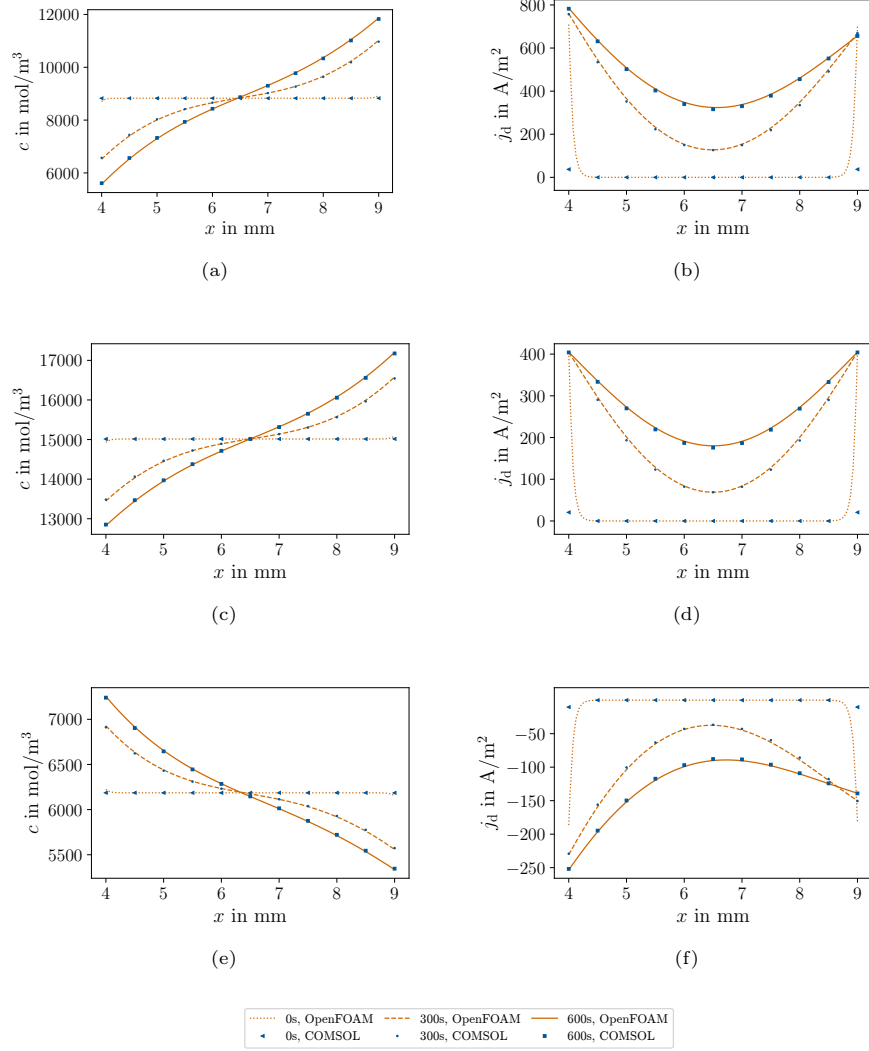


Figure S1.17: Test case 3; results for OpenFOAM and COMSOL simulations: species distribution (left) and diffusive current density (right) of the (a)&(b) Li^+ ion, (c)&(d) Cl^- ion and (e)&(f) K^+ ion.

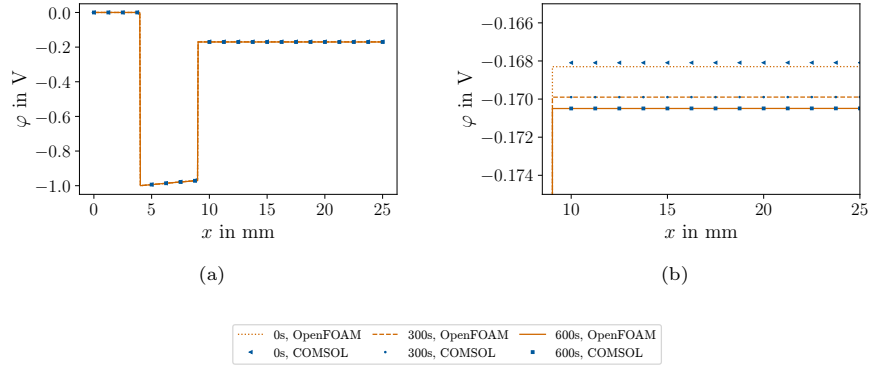


Figure S1.18: Test case 4; results for OpenFOAM and COMSOL simulations: potential distribution in the (a) whole cell and (b) anode.

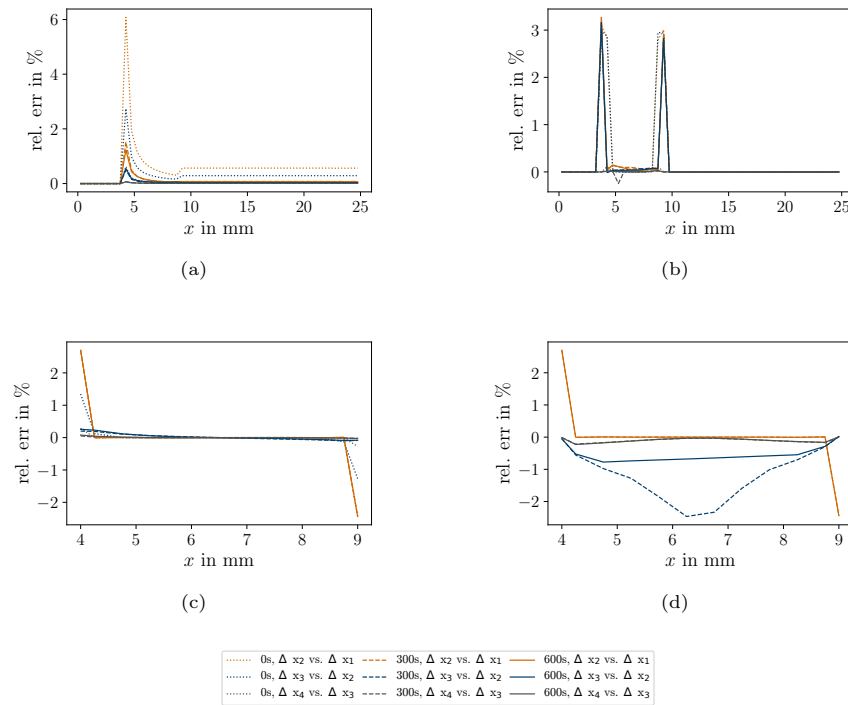


Figure S2.19: Grid study with OpenFOAM using simulation test case 3: relative error in the (a) potential distribution, (b) potential gradient, (c) species distribution of Li^+ and the (d) species gradient of Li^+ .

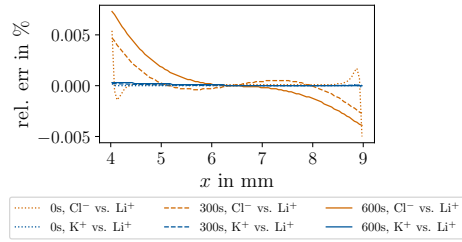


Figure S3.20: Electroneutrality study in OpenFOAM using simulation test case 3: relative error in the electric conductivity. Calculating Li^+ from electroneutrality was taken as reference.

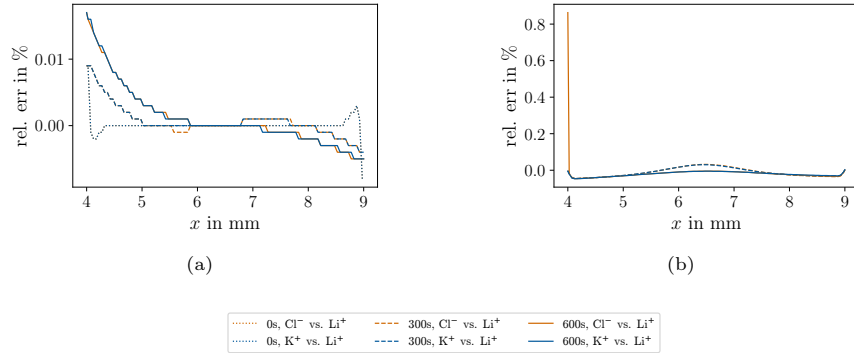


Figure S3.21: Electroneutrality study in OpenFOAM using simulation test case 3: relative error in the (a) species distribution of Li^+ and the (b) species gradient of Li^+ . Calculating Li^+ from electroneutrality was taken as reference.